# On the effectiveness of adversarial training against common corruptions

Klim Kireev[*]
EPFL
klim.kireev@epfl.ch

Maksym Andriushchenko[*]
EPFL
maksym.andriushchenko@epfl.ch

Nicolas Flammarion
EPFL
nicolas.flammarion@epfl.ch

## Abstract

The literature on robustness towards common corruptions shows no consensus on whether adversarial training can improve the performance in this setting. First, we show that, when used with an appropriately selected perturbation radius, $\ell_p$ adversarial training can serve as a strong baseline against common corruptions. Then we explain why adversarial training performs better than data augmentation with simple Gaussian noise which has been observed to be a meaningful baseline on common corruptions. Related to this, we identify the $\sigma$-*overfitting* phenomenon when Gaussian augmentation overfits to a particular standard deviation used for training which has a significant detrimental effect on common corruption accuracy. We discuss how to alleviate this problem and then how to further enhance $\ell_p$ adversarial training by introducing an *efficient relaxation* of adversarial training with *learned perceptual image patch similarity* as the distance metric. Through experiments on CIFAR-10 and ImageNet-100, we show that our approach does not only improve the $\ell_p$ adversarial training baseline but also has cumulative gains with data augmentation methods such as AugMix, ANT, and SIN leading to state-of-the-art performance on common corruptions. The code of our experiments is publicly available at https://github.com/tml-epfl/adv-training-corruptions.

## 1  Introduction

Despite achieving human-level performance on many computer vision tasks, deep neural networks are still not as robust as humans towards various distribution shifts (Szegedy et al., 2014; Dodge & Karam, 2017; Taori et al., 2020) including common image corruptions (Geirhos et al., 2018; Hendrycks & Dietterich, 2019a). Attempts to understand the vulnerability towards such shifts include analysis of the network architecture (Azulay & Weiss, 2019), the features contained in the data (Jetley et al., 2018; Ilyas et al., 2019), and frequency analysis of neural networks (Yin et al., 2019; Ortiz-Jimenez et al., 2020). Many approaches have been suggested to improve their robustness to these shifts including approaches based on
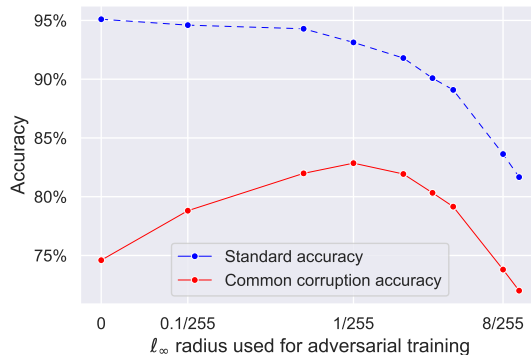


Figure 1: Accuracy on common corruptions from CIFAR-10-C for ResNet-18 models adversarially trained using different $\ell_\infty$ radii. We observe that the performance with $\varepsilon = 1/255$ is significantly higher than with the standardly used $\varepsilon = 8/255$.

---

[*]Equal contribution.

1

data augmentations (Cubuk et al., 2019; Hendrycks et al., 2019b), adversarial training (Goodfellow et al., 2015; Madry et al., 2018; Laidlaw et al., 2021), and pretraining (Hendrycks et al., 2019a).

Although data augmentation methods tend to improve the performance under common synthetic corruptions (Hendrycks et al., 2019b), these augmentations are often ad hoc and may have substantial overlap with the corruptions evaluated at test time. At the same time, there is a large amount of literature on adversarial training with $\ell_p$-bounded perturbations (Goodfellow et al., 2015; Madry et al., 2018). Adversarial training emerged as a principled approach to improve the worst-case performance of the model against *small $\ell_p$* perturbations. However, common image corruptions have a very high $\ell_p$ distance from clean samples, so the utility of using $\ell_p$ adversarial training for them is not obvious. This leads us to explore in more detail the following question:

*Can adversarial training improve the performance under common image corruptions?*

**Contributions.** We make the following contributions in our paper:

- We show that $\ell_p$ adversarial training with an *appropriately selected* perturbation radius can already serve as a strong baseline against common image corruptions.

- We compare $\ell_p$ adversarial training to Gaussian data augmentation and analyze why the latter can lead to suboptimal performance on common corruptions. We observe that it can overfit to the variance of the Gaussian noise it has been trained on which we refer to as *σ-overfitting* which, however, can be mitigated by augmenting fewer training samples.

- We introduce an efficient relaxation of adversarial training with *learned perceptual image patch similarity* (LPIPS) (Zhang et al., 2018b) based on layerwise adversarial perturbations. This new relaxation is at least as effective as previous approaches (Laidlaw et al., 2021) but significantly faster to train.

- We show that our relaxation approach has cumulative gains with existing data augmentation methods such as AugMix, ANT, and SIN leading to state-of-the-art performance on common corruptions from ImageNet-100-C.

## 2   Related work

We provide here an overview of relevant works on common image corruptions, different data augmentation methods proposed to improve the performance on corruptions, and then we discuss papers on adversarial robustness with respect to both $\ell_p$ and non-$\ell_p$ perturbations.

**Common corruptions.** Dodge & Karam (2017) first find that despite being on par with the human vision on standard images, deep networks perform suboptimally on common corruptions such as noise and blur. Geirhos et al. (2018) measure the performance of deep networks on 12 different image corruption types but find that data augmentation on one type of corruption does not tend to improve the performance on others. However, these findings are reconsidered in Rusak et al. (2020) where Gaussian data augmentation is shown to help for a wide range of image corruptions. In a standardization effort, Hendrycks & Dietterich (2019a) introduce a few image classification datasets—in particular, CIFAR-10-C and ImageNet-C—with 15 different common corruptions from four categories: noise, blur, weather, and digital corruptions. Wong & Kolter (2021) propose to train a variational auto-encoder to learn how to generate CIFAR-10-C corruptions and use this

generative model for data augmentation and adversarial training. We note that their technique assumes knowledge of some subset of corruptions from CIFAR-10-C which differs from the setting we consider in our paper. Robey et al. (2020) also use adversarial training in the latent space of a deep generative model to learn models robust to some realistic non-$\ell_p$ bounded perturbations. Recently, Radford et al. (2021) showed that contrastive pretraining on a very large set of image-caption pairs (400 million) can substantially improve the robustness against distribution shifts.

**Data augmentations.** Data augmentation is a widely used technique to improve the generalization of machine learning models. Besides classical image transformations like random flipping or cropping, many other approaches have been proposed such as linearly interpolating between images and their labels (Zhang et al., 2018a), replacing a part of the image with either a black-colored patch (DeVries & Taylor, 2017) or a part of another image (Yun et al., 2019). If the augmentation set used to be manually crafted, the selection process can be now automatized with an automatic augmentation search (Cubuk et al., 2019). One of the best-performing methods against common corruptions is AugMix (Hendrycks et al., 2019b), which combines carefully selected augmentations with a regularization term based on the Jensen-Shannon divergence. Laermann et al. (2019) combine stability training with various input perturbations such as Gaussian noise and show an improvement on different image corruptions. Taori et al. (2020) observe that improvements on synthetic distribution shifts (such as common corruptions) do not necessarily transfer to real distribution shifts. However, Hendrycks et al. (2020) show an example when improving robustness against synthetic blurs also helps against naturally obtained blurred images.

**$\ell_p$ adversarial robustness.** Adversarial training in deep learning has been first considered in Goodfellow et al. (2015) and later framed as a robust optimization problem by Madry et al. (2018). There have been many attempts in the literature to improve standard adversarial training, and we refer to an exhaustive list of the best-performing approaches to the leaderboard from Croce et al. (2020). The state-of-the-art approach of Gowal et al. (2020) is still based on adversarial training which is enhanced by the usage of additional training data, larger models, and weight averaging.

The view that adversarial training damages or at least does not improve the performance on *common corruptions* has been prevalent in the literature (Hendrycks et al., 2019b; Rusak et al., 2020; Hendrycks et al., 2020). However, previous works directly use publicly available robust models without adjusting the perturbation radius used for adversarial training. For example, (Rusak et al., 2020) show that adversarially trained ImageNet models from Xie et al. (2019), Shafahi et al. (2019), and Shafahi et al. (2020) do not help on ImageNet-C compared to standardly trained models. However, Ford et al. (2019) report that $\ell_\infty$ adversarially trained models on CIFAR-10 from Madry et al. (2018) do lead to an improvement on CIFAR-10-C compared to a standard model. The approach of Xie et al. (2020), AdvProp, relies on $\ell_\infty$ adversarial training to improve the performance on common corruptions but they advocate the use of *auxiliary* batch normalization layers for standard and adversarial training examples. We find that similar performance can be achieved on common corruptions using vanilla adversarial training without a customized use of BatchNorm layers. Kang et al. (2019) study the robustness transfer between $\ell_p$-robust models and *adversarially optimized* elastic and JPEG corruptions. They show that $\ell_p$ adversarial training can increase robustness against these two types of adversarial perturbations, but robustness does not transfer in all the cases and sometimes may even hurt robustness against other perturbation types. Hendrycks & Dietterich (2019a) report that the Adversarial Logit Pairing method (Kannan et al.,

2018) (whose $\ell_p$-robustness is questionable, see Engstrom et al. (2018) and Mosbach et al. (2018)) enables improvements on corruptions from Tiny ImageNet-P dataset which was introduced in the same paper. Similarly, Wong & Kolter (2021) report that $\ell_2$ and $\ell_\infty$ adversarial training improve on 3 held-out corruption types (Gaussian blur, spatter, and saturate) which are, however not standard to report in the literature on common corruptions (Hendrycks & Dietterich, 2019a).

**Non-$\ell_p$ adversarial robustness.** Volpi et al. (2018) propose Lagrangian-style adversarial training in the input space and in the last layer of the network. Stutz et al. (2019) propose *on-manifold* adversarial training which is performed in the latent space of a VAE-GAN generative model. However, its success crucially depends on the quality of the generative model which could not be scaled beyond simple image recognition datasets. Wei & Ma (2020) derive generalization bounds that motivate adversarial training with respect to all layers of the network which they use to improve $\ell_p$ robustness. Recently, Laidlaw et al. (2021) provided algorithms for approximate *perceptual adversarial training* based on the LPIPS distance (Zhang et al., 2018b) which is defined via activations of a neural network. They aim at improving robustness against new types of adversarial perturbations that were unseen during training.

## 3 Performance of $\ell_p$ adversarial training on common corruptions

Here we formally introduce adversarial training and show that it can lead to non-trivial improvements in terms of accuracy on CIFAR-10-C for a small enough perturbation radius.

**Background on adversarial training.** Let $\ell(x, y; \theta)$ denote the loss of a neural network parametrized by $\theta \in \mathbb{R}^m$ on the example $(x, y) \sim D$ where $D$ is the data generating distribution. Previous works (Shaham et al., 2018; Madry et al., 2018) formalized the goal of training adversarially robust models as the following robust optimization problem:

$$\min_\theta \mathbb{E}_{(x,y)\sim D} \left[ \max_{\delta \in \Delta} \ell(x + \delta, y; \theta) \right]. \tag{1}$$

In this section, we focus on the $\ell_p$ threat model, i.e. $\Delta = \{\delta \in \mathbb{R}^d : \|\delta\|_p \leq \varepsilon, \ x + \delta \in [0, 1]^d\}$, where the adversary can change each input $x$ in an $\varepsilon$-ball around it while making sure that the input $x + \delta$ does not exceed its natural range. The most common way to solve the inner maximization problem is the *projected gradient descent* method (PGD) defined by the following recursion initialized at $\delta^{(0)}$:

$$\delta^{(t+1)} \overset{\text{def}}{=} \Pi_\Delta \left[ \delta^{(t)} + \alpha \nabla_{\delta^{(t)}} \ell(x + \delta^{(t)}, y; \theta) \right], \tag{2}$$

where $\Pi$ is the projection operator on the set $\Delta$, and $\alpha$ is the step size of PGD. Instead of the gradient $\alpha \nabla_{\delta^{(t)}} \ell(x + \delta^{(t)}, y; \theta)$, one often uses the sign update $\alpha \operatorname{sign}(\nabla_{\delta^{(t)}} \ell(x + \delta^{(t)}, y; \theta))$ for $\ell_\infty$ perturbations or the $\ell_2$ normalized update $\alpha \nabla_{\delta^{(t)}} \ell(x + \delta^{(t)}, y; \theta) / \left\| \nabla_{\delta^{(t)}} \ell(x + \delta^{(t)}, y; \theta) \right\|_2$ for $\ell_2$ perturbations. The perturbation $\delta^{(0)}$ can be initialized from any point inside $\Delta$, but is often initialized from zero, or randomly (Madry et al., 2018; Wong et al., 2020).

The one-iteration variant of PGD is known as the *fast gradient method* (FGM) when the normalized $\ell_2$ update is used and as the *fast gradient sign method* (FGSM) when the $\ell_\infty$ sign update is used (Goodfellow et al., 2015). Note that in both cases the step size is $\alpha = \varepsilon$ which leads to perturbations located on the boundary of the set $\Delta$. These methods are fast but sometimes prone

Table 1: Standard accuracy and accuracy on common corruptions of multiple methods on CIFAR-10 and ImageNet-100 datasets. $\ell_2$ adversarial training substantially improves the accuracy on corrupted samples compared to the standard model.

| Training | CIFAR-10 | | ImageNet-100 | |
|---|---|---|---|---|
| | Standard | Corrupted | Standard | Corrupted |
| Standard | 95.1% | 74.6% | 86.6% | 47.5% |
| $\ell_\infty$ adversarial | 93.3% | 82.7% | 86.5% | 47.7% |
| $\ell_2$ adversarial | 93.6% | **83.4%** | 86.3% | **48.4%** |

to *catastrophic overfitting* when the model overfits to FGM/FGSM but is not robust to iterative PGD attacks (Tramèr et al., 2018; Wong et al., 2020). This problem can be alleviated by specific regularization methods like CURE (Moosavi-Dezfooli et al., 2019; Huang et al., 2020) or GradAlign (Andriushchenko & Flammarion, 2020). However, for small enough $\varepsilon$, adversarial training with FGM/FGSM works as well as multi-step PGD (Andriushchenko & Flammarion, 2020).

**Experimental details.**   We perform experiments on two common image classification datasets: CIFAR-10 (Krizhevsky & Hinton, 2009) which has $32 \times 32$ images, and ImageNet-100 (Russakovsky et al., 2015) with $224 \times 224$ images where we take each tenth class following (Laidlaw et al., 2021). We choose ImageNet-100 since we always perform a grid search over the main hyperparameters such as the perturbation radius for adversarial training or standard deviation of Gaussian noise which would be too computationally expensive to do on the full ImageNet. For all experiments, we use the pre-activation ResNet-18 architecture (He et al., 2016). We specify the exact hyperparameters in Appendix A. We evaluate the accuracy on common corruptions using CIFAR-10-C and ImageNet-C datasets from (Hendrycks & Dietterich, 2019a) which contain 15 different synthetic corruptions in 4 categories: blur, noise, digital, weather corruptions. We report the accuracy by averaging over all 5 corruption levels. The code of our experiments is publicly available[1].

**Adversarial training with small perturbations.**   While larger $\ell_p$-perturbations can be interesting for security-driven applications (Tramèr et al., 2019; Saadatpanah et al., 2020), it is not a realistic threat model for most computer vision tasks (Gilmer et al., 2018). Next, we show that the selection of the perturbation radius $\epsilon$ crucially impacts the performance on common corruptions.

We start by showing in Fig. 1 the common corruption accuracy of $\ell_\infty$ adversarially trained models as it is the most widely studied setting in the literature (Madry et al., 2018) and has been reported multiple times in common corruption literature (Hendrycks et al., 2019b; Ford et al., 2019; Rusak et al., 2020). Since we are interested primarily in small-$\varepsilon$ adversarial training, we rely throughout the paper on FGM/FGSM for $\ell_2/\ell_\infty$ norms respectively to solve the inner maximization problem (1) which only leads to a $2\times$ computational overhead. Note however that we exceptionally use PGD with 10 steps for $\varepsilon \in \{8/255, 10/255\}$ to prevent catastrophic overfitting (Wong et al., 2020) and allow a direct comparison with previous works. We observe that for the small-$\varepsilon$ regime around $\varepsilon = 1/255$, we get a significant improvement in terms of the CIFAR-10-C accuracy. Namely, we get 74.5% accuracy with standard training, 82.7% with adversarial training using $\varepsilon = 1/255$, and 73.8% using the standardly reported threshold $\varepsilon_\infty = 8/255$[2]. The reason is that the tradeoff between robustness

---

[1]https://github.com/tml-epfl/adv-training-corruptions

[2]Absolute numbers differ from (Ford et al., 2019) because we use ResNet-18 instead of WRN-28-10 and different training hyperparameters.

and accuracy (Tsipras et al., 2019) have to be carefully balanced—if the standard accuracy drops for higher $\varepsilon$, the corruption accuracy also deteriorates. Thus, the goal of achieving maximal $\ell_p$ and corruption robustness are not completely aligned, and selecting the most robust $\ell_p$-model does not necessarily lead to good performance on common corruptions. Alternatively, one can also balance this tradeoff by mixing clean and adversarial samples (Goodfellow et al., 2015), but we note that it overall leads to similar results, e.g. for $\ell_\infty$ training with 50% adversarial samples in each batch we get 82.4% accuracy on CIFAR-10-C while with 100% adversarial samples we get 82.7% accuracy for the best $\ell_\infty$ $\varepsilon$ taken out of a grid search in each case (see Appendix B for details). Thus, we focus on adversarial training with 100% adversarial samples for the rest of the paper.

We further compare the performance of different $\ell_p$ threat models. In Table 1 we report results of standard, $\ell_\infty$, and $\ell_2$ adversarial training on CIFAR-10 and ImageNet-100 where we perform a detailed grid search for each model over the perturbation radius $\varepsilon$. To the best of our knowledge, we show for the first time that adversarial training helps on ImageNet-C, and not only on CIFAR-10-C (Ford et al., 2019), improving the corruption accuracy from 47.5% to 48.4%. We observe that $\ell_2$ adversarial training performs better than $\ell_\infty$, thus we focus on this threat model in the next section.

## 4 A comparison of adversarial training and Gaussian augmentation on common corruptions

In this section, we compare $\ell_2$ adversarial training to other natural baselines including Gaussian data augmentation—which has been observed to be a meaningful baseline against common corruptions—and discuss important conceptual differences between adversarial training and the other baselines.

**A comparison across corruption types.** We compare $\ell_2$ adversarial training with a few simple baselines: standard training, gradient regularization (Drucker & LeCun, 1992), and standard Gaussian data augmentation. To ensure a fair comparison, we perform a grid search for each method (except standard training) over the perturbation radius $\varepsilon$, regularization parameter $\lambda$, and noise standard deviation $\sigma$ respectively. We choose to compare to gradient regularization since it is an established regularization method that may have a similar effect to adversarial training with small perturbations (Simon-Gabriel et al., 2019). We aggregate the corruptions over each type (blurs, digital, noise, weather) and plot the results in Fig. 2 and report results over each corruption in Fig. 10 in the Appendix.



Figure 2: Accuracy for different corruption types on CIFAR-10-C. Unlike other methods, adversarial training improves the performance on each corruption type compared to standard training.

First, we observe that adversarial training is the best performing method (83.4% corruption accuracy) followed by Gaussian augmentation (80.5%), gradient regularization (78.3%), and standard training (74.6%). We further observe that unlike other methods, $\ell_2$ adversarial training helps for *each* corruption type. At the same time, Gaussian augmentation *degrades* the performance on digital and weather corruptions while very significantly improving the performance for noise corruptions which is not surprising since the Gaussian noise used for training is also contained in the noise corruptions. Interestingly, for the fog and contrast corruptions, the performance degrades for *all*
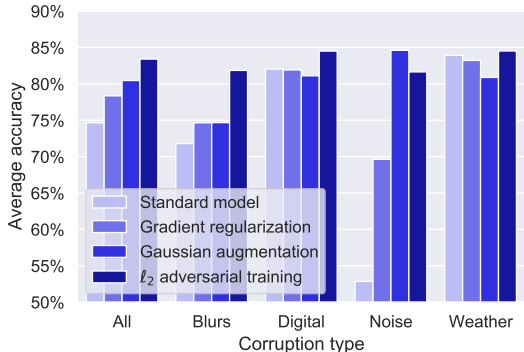
6

methods (see Table 10 in the Appendix), consistently with the observation made in Ford et al. (2019). Our results also suggest that the impact of gradient regularization on common corruption performance is limited. Therefore it cannot explain the accuracy gains of both adversarial training and Gaussian augmentation as one could have expected from the fact that these methods are equivalent to gradient regularization when used with *sufficiently* small parameters $\sigma$ and $\varepsilon$ (Bishop, 1995; Simon-Gabriel et al., 2019).

**Worst-case vs average-case behavior.** Ford et al. (2019) show that the robustness to Gaussian noise and adversarial perturbations are closely related. More precisely, they show using concentration of measure arguments that a non-zero error rate under Gaussian perturbation implies the existence of small adversarial perturbations and consequently that improving adversarial robustness leads to an improvement in robustness against Gaussian perturbations. This finding is consistent with what we observe here. What remains to be understood is why adversarial training performs *better* than Gaussian augmentation on common corruptions. The main difference between both methods appears when looking at the objectives that both methods minimize. When evaluated on a single observation $x$, the loss function considered in Gaussian augmentation is:

$$\mathbb{E}_{d \sim N(0, I\sigma^2)} \left[ \ell(\theta, x + d) \right] \ \sim \ \mathbb{E}_{\rho: ||\rho||_2 = \sigma\sqrt{d}} \left[ \ell(\theta, x + \rho) \right],$$

since Gaussian vectors with variance $\sigma^2 I$ are highly concentrated on the sphere of radius $\sigma\sqrt{d}$ in high dimensions. Therefore Gaussian augmentation amounts to minimize an *averaged* objective where perturbations are averaged over the sphere. At the other end, the objective behind adversarial training defined in Eq. (1) amounts to minimize a *worst-case* loss where the worst perturbation in the ball is considered. The crucial difference is that the minimization of the expected value of the loss function *does not guarantee* any behavior inside the sphere.

**$\sigma$-overfitting.** To investigate this behavior, we perform the following experiment in Fig. 3. For random 1000 test set images from CIFAR-10, we evaluate the loss with additive Gaussian noise of $\sigma \in [0, 0.1]$ and average the loss function over both images and perturbations for (1) a standard model, (2) a model trained with Gaussian augmentation with $\sigma = 0.05$ where all 100% training samples are augmented, (3) a model trained with Gaussian augmentation for $\sigma = 0.1$ where only 50% training samples are augmented, and (4) $\ell_2$ adversarially trained model with $\varepsilon = 0.1$. We notice that the loss function for 100% Gaussian augmentation is minimal at $\sigma$ which is only slightly less than $\sigma = 0.05$ used for its training. *Hence, the model has overfitted not only to the type of noise but also to its magnitude.* The loss function outside *and inside* of the sphere is bigger than on its surface. However, there is a simple fix if we train with 50% Gaussian noise in each batch, as suggested, e.g., in Rusak et al. (2020) in contrast to Ford et al. (2019). This scheme allows to alleviate the $\sigma$-overfitting behavior and also achieve better accuracy on clean samples (93.2% instead of 92.5%) and, most importantly, *significantly* improve on common corruptions (85.0% instead of 80.5%). At the same time, $\ell_2$ adversarial training does not suffer from this problem and both 100% and 50% schemes work nearly equally well (details can be found in Appendix B). We provide a further discussion on $\sigma$-overfitting in Appendix C together with additional experiments on ImageNet-100 where $\sigma$-overfitting has even more noticeable behavior which is likely due to the higher input dimensionality of ImageNet.
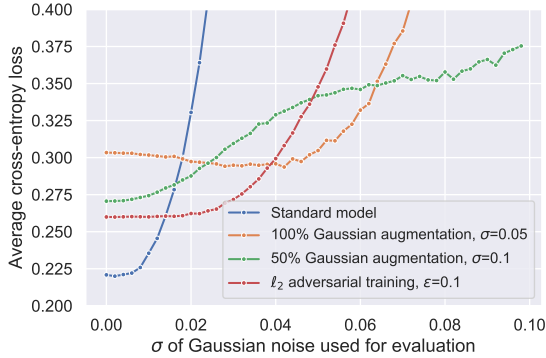
Figure 3: Average cross-entropy loss under Gaussian noise for different training methods.
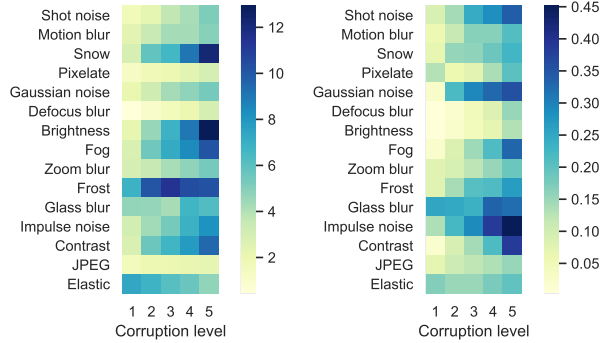
Figure 4: Average $\ell_2$ and LPIPS distance for different common corruptions from CIFAR-10-C.

**Local vs global $\ell_p$ behavior.** Interestingly, adversarial training with worst-case perturbations bounded within a small $\ell_2$ ball leads to robustness significantly beyond this radius. Fig. 4 illustrates that common corruptions have an $\ell_2$ norm an order of magnitude larger than $\varepsilon = 0.1$ used for $\ell_2$ adversarial training. This is in contrast with adversarial robustness that does not significantly extend beyond the radius used for training (Madry et al., 2018). Related to this, Ford et al. (2019) argue that *for Gaussian noise* improving the minimum distance to the decision boundary (e.g. via adversarial training) also leads to an improvement of the average distance. We believe that we have a similar mechanism at play for adversarial $\ell_2$ perturbations and common corruptions and that it may explain the generalization of adversarial training to large average-case perturbations such as those from CIFAR-10-C. However, we have a more complex setting compared to Ford et al. (2019) since at the training and test time we deal with *different* and *very diverse* types of noise.

## 5 Towards efficient perceptual adversarial training

As shown in the previous section, $\ell_2$ adversarial training already leads to encouraging results on common corruptions. We explore next how much we can improve the results of adversarial training by using a non-$\ell_p$ distance which better captures the perceptual similarity between images.

### 5.1 LPIPS distance for common corruptions

**Definition of LPIPS.** One of the main disadvantages of $\ell_p$-norms is that they are very sensitive under simple transformations such as rotations or translations (Sharif et al., 2018). One possible solution is to consider distances[3] which capture these invariances better such as the *learned perceptual image patch similarity* (LPIPS) distance introduced in Zhang et al. (2018b) and which is based on the activations of a convolutional neural network evaluated on two different images. For a convolutional neural network, the LPIPS distance is formally defined as:

$$d_{\text{LPIPS}}(x, x')^2 = \sum_{l=1}^{L} \alpha_l \|\phi_l(x) - \phi_l(x')\|_2^2, \tag{3}$$

---

[3]Not necessarily distances in a strict mathematical sense that assumes a certain set of axioms to hold.

Table 2: Correlation between distances and error rates of a standard model taken across different corruption severities and averaged over multiple corruptions. LPIPS distance is better correlated with the error rates on different corruption severity levels.

| Metric | Corruption type | | | | |
|--------|------|-------|------|---------|---------|
| | All | Noise | Blur | Weather | Digital |
| $\ell_2$ | 0.807 | **0.998** | 0.986 | 0.835 | 0.561 |
| LPIPS | **0.963** | 0.993 | **0.994** | **0.968** | **0.921** |

where $L$ is the depth of the network, $\phi_l$ is its feature map up to the $l$-th layer, and $\{\alpha_l\}_{l=1}^{L}$ are some constants that weigh the contributions of the $\ell_2$ distances between activations.

**Suitability of LPIPS for common corruptions.** We first show that the LPIPS distance is more suitable to common image corruptions than the $\ell_2$ distance. We note that previous works (Zhang et al., 2018b; Laidlaw et al., 2021) have discussed its advantages over other commonly used distances, however not in the context of corruptions from CIFAR-10-C. Another difference to Zhang et al. (2018b) is that here we compute the LPIPS distance using *full images* instead of smaller image patches as we are eventually interested in performing adversarial training using full inputs.

We compute the average $\ell_2$ and LPIPS distances based on a standardly trained VGG network using the code from Zhang et al. (2018b) for different corruptions from CIFAR-10-C. The results are shown in Fig. 4 (see also Table 12 in the Appendix), where we observe that for certain corruptions, LPIPS clearly demonstrates a more preferable behavior than the $\ell_2$ distance. For example, the $\ell_2$ distances of elastic transformations are monotonically *decreasing* over the corruption severity which is the opposite of what we would expect from a suitable distance between images. At the same time, the LPIPS distance is first slightly decreasing and then increasing which is a better behavior compared to $\ell_2$. Similarly, the $\ell_2$ distances for JPEG corruption appear to be roughly constant while they are noticeably increasing for LPIPS. The LPIPS distances for the frost corruption start from a low value and then monotonically increase whereas the $\ell_2$ distances start from a very high value and then fail to be monotonic. At the same time, LPIPS behavior is more unexpected on noise corruption where it shows a very fast increase for impulse, Gaussian, and shot noises.

Therefore, the LPIPS distance appears to better capture the severity of these corruptions. To investigate further this qualitative assessment, we compute the correlation between the $l_2$ and the LPIPS distances and the error rates of a standardly trained model (shown in Fig. 9 in the Appendix) in Table 2. More precisely, each corruption has five severity levels for which both the average distance value and the average error rate can be calculated. Therefore, for a given corruption, we compute the correlation between the vector composed of the distances corresponding to each severity level and the error-rate vector defined similarly. We take then the average correlation over each corruption type. We observe that the LPIPS distance is *more correlated* with the error rates for all corruption types except the noise one. The main difference comes from the digital corruptions where LPIPS leverages the monotonic behavior of the frost and elastic transform corruptions. Therefore, we conclude that LPIPS is quantifiably more suitable to capture the distance between common image corruptions.

## 5.2 Relaxation of LPIPS adversarial training

**LPIPS adversarial training.** In view of the positive features of LPIPS, adversarial training using LPIPS appears to be a promising approach to improve the performance on common corruptions. The worst-case loss problem considered in (1) using the LPIPS distance can be formulated as:

$$\max_{\delta} \ell(x + \delta, y; \theta) \quad \text{s.t.} \quad \text{d}_{\text{LPIPS}}(x, x + \delta) \leq \varepsilon. \tag{4}$$

However, this optimization problem is challenging since $\text{d}_{\text{LPIPS}}$ is itself defined by a neural network, and the projection onto the LPIPS-ball—as required when using PGD to solve (4)—does not admit a closed-form expression. This problem was considered in Laidlaw et al. (2021) who propose two approximate attacks: the Perceptual Projected Gradient Descent (PPGD) and the Lagrangian Perceptual Attack (LPA). We discuss their approach in more detail in Appendix D but emphasize that they either need to perform an approximate projection which is computationally expensive or come up with some scheme for tuning the Lagrange multiplier $\lambda$ in the Lagrangian formulation. Furthermore, they suggest in both cases to use 10-step iterative attacks for approximate LPIPS adversarial training which limits the scalability of the method to large datasets such as ImageNet.

**Relaxed LPIPS adversarial training.** We propose here a relaxation of the LPIPS adversarial objective (4). For the simplicity of presentation, let us assume that the LPIPS distance is defined using a *single* intermediate layer of the network, i.e. $\text{d}_{\text{LPIPS}}(x, x') = \|\phi(x) - \phi(x')\|_2$. Then we can write a neural network $f$ as the composition the feature map $\phi$ and the remaining part of the network $f(x) = h(\phi(x))$. Then the LPIPS adversarial objective (4) becomes:

$$\max_{\delta} \ell(h(\phi(x + \delta))) \quad \text{s.t.} \quad \|\phi(x) - \phi(x + \delta)\|_2 \leq \varepsilon.$$

We first introduce the slack variable $\tilde{\delta} = \phi(x) - \phi(x + \delta)$,

$$\max_{\delta, \tilde{\delta}} \ell(h(\phi(x) + \tilde{\delta})) \quad \text{s.t.} \quad \|\tilde{\delta}\|_2 \leq \varepsilon \quad \text{and} \quad \tilde{\delta} = \phi(x) - \phi(x + \delta),$$

which we relax by dropping the constraint on the slack variable $\tilde{\delta} = \phi(x) - \phi(x + \delta)$ as

$$\max_{\tilde{\delta}} \ell(h(\phi(x) + \tilde{\delta})) \quad \text{s.t.} \quad \|\tilde{\delta}\|_2 \leq \varepsilon. \tag{5}$$

A similar relaxation can be derived when the LPIPS distance is defined using multiple layers:

$$\max_{\tilde{\delta}^{(1)}, \ldots, \tilde{\delta}^{(L)}} \ell(g_L(\ldots g_1(x + \tilde{\delta}^{(1)}) \cdots + \tilde{\delta}^{(L)})) \tag{6}$$

$$\text{s.t.} \quad \|\tilde{\delta}^{(l)}\|_2 \leq \varepsilon_l \quad \forall l \in \mathcal{L}_{LPIPS} \quad \text{and} \quad \tilde{\delta}^{(l)} = 0 \quad \forall l \notin \mathcal{L}_{LPIPS},$$

where the network is written under its compositional form $f(x) = g_L \circ \cdots \circ g_1(x)$, $\mathcal{L}_{LPIPS}$ is the set of layer indices used in LPIPS and $\varepsilon_l$ denotes the $\ell_2$ bound imposed at the $l$-th layer. We denote this relaxation as *relaxed LPIPS adversarial training* (RLAT) and solve it efficiently using a single-iteration adversarial attack similar to FGM (Goodfellow et al., 2015). We provide detailed derivations of RLAT and the precise algorithm in Appendix D together with additional implementation details.

We emphasize that the projection of each $\tilde{\delta}^{(l)}$ onto the corresponding $\ell_2$ balls is computationally cheap to perform, unlike the LPIPS projection. In all our experiments we opt to use the *same* network as the one used for classification although an external network can also possibly be used as discussed in Laidlaw et al. (2021). Finally, we remark that similar in spirit layerwise adversarial training methods have been proposed before (Stutz et al., 2019; Volpi et al., 2018; Wei & Ma, 2020). However, viewing layerwise adversarial training as an efficient relaxation of LPIPS adversarial training is novel, as well as applying these methods for general robustness such as common corruptions.

**LPIPS robustness of RLAT.** Since our proposed method is only a relaxation of LPIPS adversarial training, it is natural to ask whether it improves the LPIPS robustness. For this, we use the Lagrangian Perceptual Attack attack developed in Laidlaw et al. (2021) to measure LPIPS adversarial accuracy under different LPIPS radii and plot results in Fig. 5 on CIFAR-10. We use standard, $\ell_2$ adversarial training (AT), Fast perceptual AT, and RLAT models with their main hyperparameters selected to perform best on common corruptions.[4] We observe that our relaxed LPIPS adversarial training indeed substantially improves LPIPS



Figure 5: LPIPS adversarial robustness of different training schemes on CIFAR-10.

adversarial accuracy, even more than other approaches such as $\ell_2$ AT and Fast perceptual AT. We also provide a similar evaluation for $\ell_2$ robustness in Appendix D (Fig. 8).
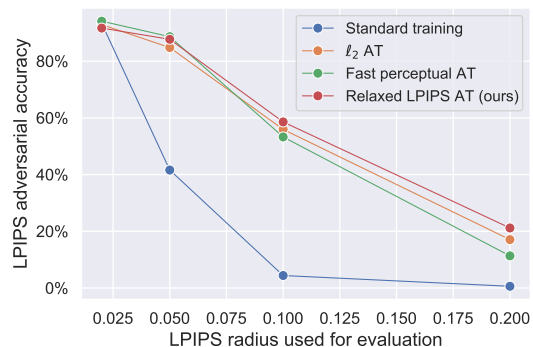
# 6 Experimental evaluation

Here we evaluate the performance of RLAT compared to other established methods and show that RLAT can be also successfully combined with different data augmentation methods.

**Experimental setup.** We compare the results for our method with additional baselines: $\ell_2$ and $\ell_\infty$ adversarial training (with 100% adversarial samples per batch), Gaussian augmentation (with both 50% and 100% augmentations per batch), AdvProp (Xie et al., 2020), fast perceptual adversarial training (Fast PAT) (Laidlaw et al., 2021), and also three data augmentation approaches: AugMix (Hendrycks et al., 2019b), adversarial noise training (ANT) (Rusak et al., 2020), and Stylized ImageNet (SIN) (Geirhos et al., 2019). We train all methods from random initialization except ANT where we follow the scheme of Rusak et al. (2020) that involves fine-tuning a standard pretrained model. We use AugMix data augmentation without the regularization term (and thus mark it as *AugMix (no JSD loss)*) since the main improvement comes from the augmentation method itself as Hendrycks et al. (2019b) report in their ablation studies. We believe that this regularization term can further improve the results independently of the augmentation. All comparisons between methods are performed with a grid search over their main hyperparameters such as $\sigma$ in Gaussian augmentation or $\epsilon$ in adversarial training. The full results for different hyperparameters in the grid

---

[4]We note that Laidlaw et al. (2021) rather focus on robustness to unseen *adversarial* examples that involve a worst-case optimization process, while we focus on unseen common corruptions taken from fixed datasets. This is the reason why the optimal perturbation radii for adversarial training (both using $\ell_p$ and LPIPS distances) that we consider are in general noticeably smaller than what Laidlaw et al. (2021) report in their paper.

Table 3: Standard and common corruption accuracy of different methods on CIFAR-10. Gray-colored numbers correspond to methods that were at least partially trained with the corruptions from CIFAR-10-C.

| | Accuracy | |
|---|---|---|
| **Method** | Standard | Corrupted |
| Standard training | 95.1% | 74.6% |
| Gradient regularization | 93.4% | 78.8% |
| 100% Gaussian augmentation | 92.5% | 80.5% |
| 50% Gaussian augmentation | 93.2% | 85.0% |
| Fast PAT | 93.4% | 82.4% |
| $\ell_\infty$ AT | 93.3% | 82.7% |
| AdvProp | 94.7% | 82.9% |
| $\ell_2$ AT | 93.6% | 83.4% |
| Relaxed LPIPS AT | 93.1% | **84.1%** |
| AugMix (no JSD loss) | 95.0% | 86.9% |
| AugMix (no JSD loss) + Relaxed LPIPS AT | 94.8% | **88.5%** |

are shown in Appendix A. For Fast PAT on CIFAR-10, we do a grid search over their parameter $\varepsilon$, but on ImageNet-100 we report the results based on the models provided by the authors since due to our limited computational resources, it is not feasible to run a proper grid search over $\varepsilon$ (each model takes 5 days of training on 4 Nvidia RTX 2080 Ti GPUs). More details can be found in our repository https://github.com/tml-epfl/adv-training-corruptions.

**Overlapping augmentations.** As data augmentation, we use only random horizontal flip and random crops which do not overlap with the corruptions from CIFAR-10-C and ImageNet-100-C. Moreover, when we train Fast PAT on CIFAR-10, we make sure to remove the overlapping augmentations used in the robustness library (Engstrom et al., 2019) such as random brightness and contrast change. In the case of AugMix, as mentioned in Rusak et al. (2020), there is a visual similarity, e.g., between the posterize operation and the JPEG corruption, but as with other augmentations, it is hard to quantify the overlap between augmentations used for training and testing. We do not compare to black-box noise generators such as DeepAugment (Hendrycks et al., 2020) since there is no guarantee that the produced noise does not have substantial overlap with common corruptions. At the same time, we emphasize that concerning overlapping augmentations, RLAT is very different since most of the perturbation is performed *inside* the layers of the network, and the part of the perturbation which is applied in the input space has a small $\ell_p$-norm.

**Discussion of experimental results.** We show the main experimental results in Table 3 on CIFAR-10-C and in Table 4 on ImageNet-100-C. First, we observe that $\ell_p$ adversarial training is a strong baseline on common corruptions on both datasets with a larger gain on CIFAR-10-C. Using our proposed relaxed LPIPS adversarial training further improves the corruption accuracy on both datasets: from 74.6% to 84.1% on CIFAR-10-C and from 47.5% to 48.8% compared to standard models. We also observe that 100% Gaussian augmentation even deteriorates the performance on ImageNet-100-C while 50% Gaussian augmentation significantly improves the average accuracy which is consistent with Rusak et al. (2020). AdvProp performs similarly to $\ell_\infty$ and worse than $\ell_2$ adversarial training while having better clean accuracy which is expected since their approach is focused on improving the standard accuracy and at test time uses BatchNorms obtained from

Table 4: Standard and common corruption accuracy of different methods on ImageNet-100. Gray-colored numbers correspond to methods that were at least partially trained with the corruptions from ImageNet-100-C.

| Method | Accuracy | |
|---|---|---|
| | Standard | Corrupted |
| Standard training | 86.6% | 47.5% |
| 100% Gaussian augmentation | 86.4% | 46.7% |
| 50% Gaussian augmentation | 83.8% | 55.2% |
| Fast PAT | 71.5% | 45.2% |
| $\ell_\infty$ AT | 86.5% | 47.7% |
| $\ell_2$ AT | 86.3% | 48.4% |
| Relaxed LPIPS AT | 86.5% | **48.8%** |
| AugMix (no JSD loss) | 86.7% | 52.3% |
| AugMix (no JSD loss) + Relaxed LPIPS AT | 86.8% | **54.8%** |
| SIN | 86.6% | 53.7% |
| SIN + Relaxed LPIPS AT | 86.5% | **54.3%** |
| ANT$^{3x3}$ | 85.9% | 57.7% |
| ANT$^{3x3}$ + Relaxed LPIPS AT | 85.3% | **58.3%** |

standard training examples. Since the performance of AdvProp on CIFAR-10-C is similar to that of $\ell_p$ adversarial training, we do not benchmark it on ImageNet-100-C.

Moreover, we observe that our proposed RLAT can be successfully combined with existing data augmentations. For example, combining the AugMix augmentation with RLAT helps to improve the accuracy on CIFAR-10-C from 86.9% to 88.5% and on ImageNet-100-C from 52.3% to 54.8%. Combining SIN and ANT$^{3x3}$ improves the accuracy on ImageNet-100-C from 53.7% to 54.3% and from 57.7% to 58.3% respectively. Thus, we conclude that RLAT is not only a helpful technique on its own but it can also benefit from advanced data augmentations.

We provide additional experimental results in the Appendix. In Section E, we evaluate the performance of the models from Table 4 on ImageNet-A, ImageNet-R, and Stylized ImageNet to better understand how well the improvements on common corruptions transfer to other distribution shifts. In Section F, we provide more detailed experimental results such as those presented in Tables 3 and 4 but with breakdowns over different corruptions and severity levels.

**Runtime of Relaxed LPIPS AT.** With the same PreAct ResNet-18 architecture, RLAT achieves a significant speed-up over Fast PAT: 1.8 hours vs 9.4 hours of wallclock time on CIFAR-10. In addition, the runtime of RLAT is not much higher than the runtime of $\ell_2 / \ell_\infty$ adversarial training (1.8 hours vs 1.3 hours on CIFAR-10) and clean training (0.8 hours on CIFAR-10). On ImageNet-100, RLAT takes 6.2 hours on a single V100 GPU. This can be compared to 120 hours (5 days) using 4 Nvidia RTX 2080 Ti GPUs for Fast PAT as reported in Laidlaw et al. (2021), although they use a larger network (ResNet-50 vs ResNet-18). We report a full runtime comparison between standard training, $\ell_2 / \ell_\infty$ adversarial training, RLAT, and Fast PAT in Table 8 in the Appendix. These runtimes show further the advantage of the single-step adversarial training procedure of RLAT compared to the multi-step approach of Fast PAT. It would be interesting in future work to develop a single-step version of Fast-LPA which is, however, not straightforward because of their Lagrangian formulation and the need to tune the parameter $\lambda$ over the iterations of Fast-LPA.

# 7 Conclusions and future work

Our findings suggest that adversarial training can be successfully used to improve the performance on common image corruptions. Even simple $\ell_p$ adversarial training can serve as a strong baseline if the optimal perturbation radius $\varepsilon$ is carefully chosen for the given problem. More advanced adversarial training schemes involve perceptual distances, such as LPIPS, and we provide a relaxation of LPIPS adversarial training with an efficient single-step procedure for adversarial training. We observe that the developed relaxation substantially improves the LPIPS robustness and can be successfully combined with existing data augmentations. We hope that the developed relaxed LPIPS adversarial training would be of interest also for other domains such as natural language processing where robustness to commonly occurring corruptions (e.g., typos) is an important task.

However, despite various data augmentation methods have been proposed in the literature against common corruptions, we believe that future work has to better clarify which augmentations have substantial overlap with common corruptions. While the overlap is clear when the *same distribution* is used at training and test time—such as Gaussian augmentation (Rusak et al., 2020)—it is less clear for black-box augmentations, e.g., those that are generated via some neural network. Developing formal criteria to determine which augmentations overlap appears to be important for further progress in the field.

Additionally, some variations of adversarial training—such as FGSM training with a large perturbation radius—are known to suffer from a phenomenon called *catastrophic overfitting* (Tramèr et al., 2018; Wong et al., 2020) when a model overfits to a particular perturbation type used during training. Catastrophic overfitting shares *some* similarities with the $\sigma$-overfitting phenomenon that we discussed in our paper. Clarifying the relation of catastrophic overfitting and $\sigma$-overfitting is another interesting direction for future work.

## Acknowledgments

## References

Andriushchenko, M. and Flammarion, N. Understanding and improving fast adversarial training. In *NeurIPS*, 2020.

Azulay, A. and Weiss, Y. Why do deep convolutional networks generalize so poorly to small image transformations? *JMLR*, 20(184):1–25, 2019.

Bishop, C. M. Training with noise is equivalent to Tikhonov regularization. *Neural Computation*, 7(1): 108–116, January 1995.

Croce, F. and Hein, M. Reliable evaluation of adversarial robustness with an ensemble of diverse parameter-free attacks. In *ICML*, 2020.

Croce, F., Andriushchenko, M., Sehwag, V., Flammarion, N., Chiang, M., Mittal, P., and Hein, M. Robustbench: a standardized adversarial robustness benchmark. *arXiv preprint arXiv:2010.09670*, 2020.

Cubuk, E. D., Zoph, B., Mane, D., Vasudevan, V., and Le, Q. V. Autoaugment: Learning augmentation policies from data. In *CVPR*, 2019.

DeVries, T. and Taylor, G. W. Improved regularization of convolutional neural networks with cutout. *arXiv preprint arXiv:1708.04552*, 2017.

Dodge, S. and Karam, L. A study and comparison of human and deep learning recognition performance under visual distortions. In *ICCCN*, 2017.

Drucker, H. and LeCun, Y. Improving generalization performance using double backpropagation. *IEEE Transactions on Neural Networks*, 1992.

Engstrom, L., Ilyas, A., and Athalye, A. Evaluating and understanding the robustness of adversarial logit pairing. *NeurIPS 2018 Workshop on Security in Machine Learning*, 2018.

Engstrom, L., Ilyas, A., Salman, H., Santurkar, S., and Tsipras, D. Robustness (python library), 2019. URL https://github.com/MadryLab/robustness.

Ford, N., Gilmer, J., Carlini, N., and Cubuk, D. Adversarial examples are a natural consequence of test error in noise. In *ICML*, 2019.

Geirhos, R., Temme, C. R. M., Rauber, J., Schütt, H. H., Bethge, M., and Wichmann, F. A. Generalisation in humans and deep neural networks. In *NeurIPS*, 2018.

Geirhos, R., Rubisch, P., Michaelis, C., Bethge, M., Wichmann, F. A., and Brendel, W. Imagenet-trained CNNs are biased towards texture; increasing shape bias improves accuracy and robustness. *ICLR*, 2019.

Gilmer, J., Adams, R. P., Goodfellow, I., Andersen, D., and Dahl, G. E. Motivating the rules of the game for adversarial example research. *arXiv preprint arXiv:1807.06732*, 2018.

Goodfellow, I. J., Shlens, J., and Szegedy, C. Explaining and harnessing adversarial examples. *ICLR*, 2015.

Gowal, S., Qin, C., Uesato, J., Mann, T., and Kohli, P. Uncovering the limits of adversarial training against norm-bounded adversarial examples. *arXiv preprint arXiv:2010.03593*, 2020.

He, K., Zhang, X., Ren, S., and Sun, J. Identity mappings in deep residual networks. *ECCV*, 2016.

Hendrycks, D. and Dietterich, T. Benchmarking neural network robustness to common corruptions and perturbations. In *ICLR*, 2019a.

Hendrycks, D. and Dietterich, T. Benchmarking neural network robustness to common corruptions and perturbations. In *ICLR*, 2019b.

Hendrycks, D., Lee, K., and Mazeika, M. Using pre-training can improve model robustness and uncertainty. In *ICML*, 2019a.

Hendrycks, D., Mu, N., Cubuk, E. D., Zoph, B., Gilmer, J., and Lakshminarayanan, B. Augmix: A simple data processing method to improve robustness and uncertainty. In *ICLR*, 2019b.

Hendrycks, D., Zhao, K., Basart, S., Steinhardt, J., and Song, D. Natural adversarial examples. *arXiv preprint arXiv:1907.07174*, 2019c.

Hendrycks, D., Basart, S., Mu, N., Kadavath, S., Wang, F., Dorundo, E., Desai, R., Zhu, T., Parajuli, S., Guo, M., et al. The many faces of robustness: A critical analysis of out-of-distribution generalization. *arXiv preprint arXiv:2006.16241*, 2020.

Huang, T., Menkovski, V., Pei, Y., and Pechenizkiy, M. Bridging the performance gap between fgsm and pgd adversarial training. *arXiv preprint arXiv:2011.05157*, 2020.

Ilyas, A., Santurkar, S., Tsipras, D., Engstrom, L., Tran, B., and Madry, A. Adversarial examples are not bugs, they are features. In *NeurIPS*, 2019.

Jetley, S., Lord, N. A., and Torr, P. H. With friends like these, who needs adversaries? In *NeurIPS*, 2018.

Kang, D., Sun, Y., Brown, T., Hendrycks, D., and Steinhardt, J. Transfer of adversarial robustness between perturbation types. *arXiv preprint arXiv:1905.01034*, 2019.

Kannan, H., Kurakin, A., and Goodfellow, I. J. Adversarial logit pairing. *CoRR*, abs/1803.06373, 2018.

Krizhevsky, A. and Hinton, G. Learning multiple layers of features from tiny images. *Technical Report*, 2009.

Krizhevsky, A., Sutskever, I., and Hinton, G. Imagenet classification with deep convolutional neural networks. In *NeurIPS*, 2012.

Laermann, J., Samek, W., and Strodthoff, N. Achieving generalizable robustness of deep neural networks by stability training. In *GCPR*, 2019.

Laidlaw, C., Singla, S., and Feizi, S. Perceptual adversarial robustness: Generalizable defenses against unforeseen threat models. In *ICLR*, 2021.

Madry, A., Makelov, A., Schmidt, L., Tsipras, D., and Vladu, A. Towards deep learning models resistant to adversarial attacks. In *ICLR*, 2018.

Moosavi-Dezfooli, S.-M., Fawzi, A., Uesato, J., and Frossard, P. Robustness via curvature regularization, and vice versa. In *CVPR*, 2019.

Mosbach, M., Andriushchenko, M., Trost, T., Hein, M., and Klakow, D. Logit pairing methods can fool gradient-based attacks. *NeurIPS 2018 Workshop on Security in Machine Learning*, 2018.

Ortiz-Jimenez, G., Modas, A., Moosavi-Dezfooli, S.-M., and Frossard, P. Hold me tight! influence of discriminative features on deep network boundaries. In *NeurIPS*, 2020.

Radford, A., Kim, J. W., Hallacy, C., Ramesh, A., Goh, G., Agarwal, S., Sastry, G., Askell, A., Mishkin, P., Clark, J., et al. Learning transferable visual models from natural language supervision. 2021.

Robey, A., Hassani, H., and Pappas, G. J. Model-based robust deep learning. *arXiv preprint arXiv:2005.10247*, 2020.

Rusak, E., Schott, L., Zimmermann, R. S., Bitterwolf, J., Bringmann, O., Bethge, M., and Brendel, W. A simple way to make neural networks robust against diverse image corruptions. In *ECCV*, 2020.

Russakovsky, O., Deng, J., Su, H., Krause, J., Satheesh, S., Ma, S., Huang, Z., Karpathy, A., Khosla, A., Bernstein, M., et al. Imagenet large scale visual recognition challenge. *IJCV*, 2015.

Saadatpanah, P., Shafahi, A., and Goldstein, T. Adversarial attacks on copyright detection systems. In *ICML*, 2020.

Shafahi, A., Najibi, M., Ghiasi, A., Xu, Z., Dickerson, J., Studer, C., Davis, L. S., Taylor, G., and Goldstein, T. Adversarial training for free! In *NeurIPS*, 2019.

Shafahi, A., Najibi, M., Xu, Z., Dickerson, J., Davis, L. S., and Goldstein, T. Universal adversarial training. In *AAAI*, 2020.

Shaham, U., Yamada, Y., and Negahban, S. Understanding adversarial training: Increasing local stability of supervised models through robust optimization. *Neurocomputing*, 2018.

Sharif, M., Bauer, L., and Reiter, M. K. On the suitability of lp-norms for creating and preventing adversarial examples. In *CVPR Workshops*, 2018.

Simon-Gabriel, C.-J., Ollivier, Y., Bottou, L., Schölkopf, B., and Lopez-Paz, D. First-order adversarial vulnerability of neural networks and input dimension. *ICML*, 2019.

Stutz, D., Hein, M., and Schiele, B. Disentangling adversarial robustness and generalization. In *CVPR*, 2019.

Szegedy, C., Zaremba, W., Sutskever, I., Bruna, J., Erhan, D., Goodfellow, I., and Fergus, R. Intriguing properties of neural networks. In *ICLR*, 2014.

Taori, R., Dave, A., Shankar, V., Carlini, N., Recht, B., and Schmidt, L. Measuring robustness to natural distribution shifts in image classification. *NeurIPS*, 2020.

Tramèr, F., Dupré, P., Rusak, G., Pellegrino, G., and Boneh, D. Adversarial: Perceptual ad blocking meets adversarial machine learning. In *ACM SIGSAC CCS*, 2019.

Tramèr, F., Kurakin, A., Papernot, N., Goodfellow, I., Boneh, D., and McDaniel, P. Ensemble adversarial training: Attacks and defenses. In *ICLR*, 2018.

Tsipras, D., Santurkar, S., Engstrom, L., Turner, A., and Madry, A. Robustness may be at odds with accuracy. In *ICLR*, 2019.

Volpi, R., Namkoong, H., Sener, O., Duchi, J. C., Murino, V., and Savarese, S. Generalizing to unseen domains via adversarial data augmentation. In *NeurIPS*, 2018.

Wei, C. and Ma, T. Improved sample complexities for deep neural networks and robust classification via an all-layer margin. In *ICLR*, 2020.

Wong, E. and Kolter, J. Z. Learning perturbation sets for robust machine learning. In *ICLR*, 2021.

Wong, E., Rice, L., and Kolter, J. Z. Fast is better than free: Revisiting adversarial training. In *ICLR*, 2020.

Xie, C., Wu, Y., Maaten, L. v. d., Yuille, A. L., and He, K. Feature denoising for improving adversarial robustness. In *CVPR*, 2019.

Xie, C., Tan, M., Gong, B., Wang, J., Yuille, A. L., and Le, Q. V. Adversarial examples improve image recognition. In *CVPR*, 2020.

Yin, D., Lopes, R. G., Shlens, J., Cubuk, E. D., and Gilmer, J. A fourier perspective on model robustness in computer vision. In *NeurIPS*, 2019.

Yun, S., Han, D., Oh, S. J., Chun, S., Choe, J., and Yoo, Y. Cutmix: Regularization strategy to train strong classifiers with localizable features. In *ICCV*, 2019.

Zhang, H., Cisse, M., Dauphin, Y. N., and Lopez-Paz, D. mixup: Beyond empirical risk minimization. In *ICLR*, 2018a.

Zhang, R., Isola, P., Efros, A. A., Shechtman, E., and Wang, O. The unreasonable effectiveness of deep features as a perceptual metric. In *CVPR*, 2018b.

# Appendix

## Organization of the Appendix

The appendix contains additional implementation details for our methods and the baselines we compare to, as well as more detailed derivations and experimental results. The appendix is organized as follows:

- Section A: further details on our experimental setup, hyperparameter choice, and runtime of different methods.

- Section B: an ablation study for AdvProp comparing it to adversarial training with some fraction of clean images.

- Section C: further experiments related to $\sigma$-overfitting on ImageNet-100 and more detailed discussion.

- Section D: full derivations for our Relaxed LPIPS adversarial training method, further implementation details, and evaluation of $\ell_2$ robustness.

- Section E: evaluation of the performance of various models on different distribution shifts such as ImageNet-A, ImageNet-R, and Stylized ImageNet.

- Section F: more detailed experimental results related to Sections 4 and 6 such as breakdowns over different corruptions and severity levels.

## A    Experimental details

In this section, we provide more details regarding our experimental settings, hyperparameters, evaluation metrics, and runtime of our method.

**Dataset details.**    We perform experiments on two common image classification datasets: CIFAR-10 (Krizhevsky & Hinton, 2009) which has $32 \times 32$ images, and ImageNet-100 (Russakovsky et al., 2015) with $224 \times 224$ images where we take each tenth class according to the WordNet ID order following Laidlaw et al. (2021). We choose ImageNet-100 instead of the full ImageNet since we have limited computation resources for performing grid searches on large-scale datasets over the main hyperparameters such as the perturbation radius for adversarial training or the standard deviation of the Gaussian noise.

The CIFAR-10-C and ImageNet-C datasets that were introduced in Hendrycks & Dietterich (2019a) contain 15 main synthetic corruptions: Gaussian noise, shot noise, impulse noise, defocus blur, glass blur, motion blur, zoom blur, snow, frost, fog, brightness, contrast, elastic, pixelation, and JPEG. Both datasets contain also 4 additional corruptions (speckle noise, Gaussian blur, spatter, saturation) that are not commonly used. Each corruption has 5 levels of severity. We use the CIFAR-10-C and ImageNet-C images provided by Hendrycks & Dietterich (2019a), although one could alternatively apply the corruptions in-memory (as done, e.g., in (Ford et al., 2019)).

In addition, we make use of three more variants of ImageNet: Stylized ImageNet, ImageNet-A and ImageNet-R. Stylized ImageNet (SIN) is a variant of ImageNet which is obtained using style transfer.

It has been first introduced to induce a shape bias in convolutional networks (Geirhos et al., 2019). ImageNet-A (Hendrycks et al., 2019c) is a test set of 7 500 natural but adversarially collected images with, e.g., unusual backgrounds or occlusions for 200 ImageNet classes. ImageNet-R (Hendrycks et al., 2020) is a test set of 30 000 image renditions (e.g., paintings, sculptures, embroidery) for another set of 200 ImageNet classes. When evaluating on these datasets, we only use the classes intersecting with ImageNet-100.

**Evaluation details.** There are 15 corruptions and 5 severity levels in CIFAR-10-C and ImageNet-C. Thus there are multiple ways of reporting the performance of a model on these two datasets. For a model $f$, let $E_{s,c}^f$ denote the top-1 error rate on the corruption $c$ with severity level $s$ averaged over the whole test set, then three popular metrics are often reported:

- *Average accuracy*: the accuracy is averaged over all severity levels and corruptions:

$$\text{Accuracy}_f = 1 - \frac{1}{15 \cdot 5} \sum_{c=1}^{15} \sum_{s=1}^{5} E_{s,c}^f.$$

- *Mean corruption error* (mCE, proposed in Hendrycks & Dietterich (2019b)): the error rate on each corruption is normalized by the error rate, $E_{s,c}^{\text{AlexNet}}$, of the standard deep learning model, AlexNet (Krizhevsky et al., 2012):

$$\text{mCE}_f = \frac{1}{15} \sum_{c=1}^{15} \frac{\sum_{s=1}^{5} E_{s,c}^f}{\sum_{s=1}^{5} E_{s,c}^{\text{AlexNet}}}.$$

The motivation is to make the error rates on different corruptions more comparable. Indeed they do not all have the same inherent level of difficulty.

- *Relative mean corruption error* (relative mCE, proposed in Hendrycks & Dietterich (2019b)): instead of measuring the error rate, one can also consider the degradation of the error rate compared to the standard error rate $E_{\text{standard}}^f$ of the model $f$ taken relative to the degradation of the error rate $E_{\text{standard}}^{\text{AlexNet}}$ of AlexNet:

$$\text{Relative mCE}_f = \frac{1}{15} \sum_{c=1}^{15} \frac{\sum_{s=1}^{5} E_{s,c}^f - E_{\text{standard}}^f}{\sum_{s=1}^{5} E_{s,c}^{\text{AlexNet}} - E_{\text{standard}}^{\text{AlexNet}}}.$$

However, this metric has to be carefully interpreted since it does not take absolute accuracy into account, e.g., a *constant* model achieves the perfect score of 0 for this metric.

Table 5: The main hyperparameters used for CIFAR-10 and ImageNet experiments.

| | Dataset | |
| --- | --- | --- |
| **Hyperparameter** | CIFAR-10 | ImageNet-100 |
| Architecture | PreAct ResNet-18 | PreAct ResNet-18 |
| Number of epochs | 150 | 100 |
| Learning rate of SGD | 0.1 | 0.1 |
| Epochs for learning rate decay (by $10\times$ factor) | $\{50, 100\}$ | $\{33, 66\}$ |
| Momentum | 0.9 | 0.9 |
| Batch size | 128 | 128 |
| Weight decay | 0.0005 | 0.0005 |

Table 6: Grid searches performed for CIFAR-10 experiments. For each grid, we boldface the hyperparameter that leads to the model with the best common corruption accuracy.

| Method | Grid values |
|---|---|
| 100% Gaussian augmentation | $\sigma \in \{0.02, \mathbf{0.05}, 0.08, 0.1, 0.2\}$ |
| 50% Gaussian augmentation | $\sigma \in \{0.02, 0.05, 0.08, \mathbf{0.1}, 0.2\}$ |
| $\ell_\infty$ adversarial training | $\varepsilon \in \{0.1, 0.5, \mathbf{1.0}, 2.0, 4.0, 8.0, 16.0\}$ |
| $\ell_2$ adversarial training | $\varepsilon \in \{0.01, 0.05, 0.08, \mathbf{0.1}, 0.15, 0.2, 0.5, 1.0\}$ |
| Fast PAT | $\varepsilon \in \{0.005, 0.01, \mathbf{0.02}, 0.05, 0.08\}$ |
| AdvProp | $\varepsilon \in \{0.5, 1.0, \mathbf{2.0}, 4.0, 8.0\}$ |
| RLAT | $\varepsilon \in \{0.05, \mathbf{0.08}, 0.1, 0.15, 0.2, 0.25\}$ |

Table 7: Grid searches performed for ImageNet-100 experiments. For each grid, we boldface the hyperparameter that leads to the model with the best common corruption accuracy.

| Method | Grid values |
|---|---|
| 100% Gaussian augmentation | $\sigma \in \{\mathbf{0.001}, 0.005, 0.01, 0.02, 0.05, 0.1, 0.2, 0.4, 0.5, 0.6\}$ |
| 50% Gaussian augmentation | $\sigma \in \{0.01, 0.02, 0.05, 0.1, 0.2, \mathbf{0.5}, 0.8\}$ |
| $\ell_\infty$ adversarial training | $\varepsilon \in \{0.01, \mathbf{0.05}, 0.1, 0.5, 1.0, 2.0, 3.0, 4.0\}$ |
| $\ell_2$ adversarial training | $\varepsilon \in \{0.02, \mathbf{0.05}, 0.1, 0.2\}$ |
| RLAT | $\varepsilon \in \{0.01, \mathbf{0.02}, 0.05, 0.1, 0.2\}$ |
| RLAT + AugMix | $\varepsilon \in \{0.01, 0.02, \mathbf{0.05}, 0.1, 0.2\}$ |
| RLAT + SIN | $\varepsilon \in \{0.005, \mathbf{0.01}, 0.02, 0.05\}$ |
| RLAT + ANT$^{3x3}$ | $\varepsilon \in \{0.005, 0.01, \mathbf{0.02}, 0.05\}$ |

Since there is no standard AlexNet model on CIFAR-10, the mean corruption error and the relative mean corruption error are not well defined on this dataset. Therefore we focus on reporting average accuracy on both CIFAR-10-C and ImageNet-100-C to be consistent throughout the paper.

For the LPIPS robustness evaluation shown in Fig. 5, we use the following settings: Fast Lagrangian Attack from Laidlaw et al. (2021) using their suggested hyperparameters and AlexNet as the network to compute the LPIPS distance. For the $\ell_2$ robustness evaluation, we use the APGD-CE attack (Croce & Hein, 2020) with 100 iterations and 5 random restarts.

**Training details.** In all our experiments, we use SGD with momentum to train a PreAct ResNet-18 network (both on CIFAR-10 and ImageNet-100). The momentum coefficient is set to the value 0.9. The learning rate is initially set to the value 0.1 and then is decayed by a factor 10 according to a predefined schedule. We train for 150 epochs on CIFAR-10 and 100 epochs on ImageNet-100 and always report the results of the *last* model, i.e. we do not perform any early stopping. We specify all the main training hyperparameters in Table 5.

In all experiments, we use random horizontal flip and random crops as data augmentation methods. For the experiments whose results are reported in Tables 3 and 4, we use additional augmentations like AugMix, SIN, ANT$^{3x3}$ whenever it is explicitly mentioned.

For every method that we reported, we performed a grid search over the main hyperparameters such as the standard deviation $\sigma$ for Gaussian data augmentation or the perturbation radius $\varepsilon$ for adversarial training. We report all the used grids in Table 6 and Table 7. We note that the grids are not of the same size for all methods since in case an initial grid of values came out to be suboptimal, we expanded it further until the optimal value (according to common corruption accuracy) was attained not at the boundary of the grid. The only exception is for 100% Gaussian augmentation on ImageNet-100 in Table 7 where the best performance is attained for the smallest $\sigma = 0.001$ out

Table 8: Wall-clock time in hours for PreAct ResNet-18 trained with different methods on CIFAR-10 and ImageNet-100 using one Nvidia V100 GPU. [*] denotes the time reported by Laidlaw et al. (2021) for a larger model (ResNet-50) using different hardware (4 Nvidia RTX 2080 Ti GPUs).

| | **Dataset** | |
| Training | CIFAR-10 | ImageNet-100 |
| --- | --- | --- |
| Standard | 0.8h | 3.9h |
| $\ell_2/\ell_\infty$ adversarial | 1.3h | 5.8h |
| Relaxed LPIPS AT | 1.8h | 6.2h |
| Fast PAT | 9.4h | [*]120h |

of the final grid. We found out that even such a small $\sigma$ still harms the overall performance due to $\sigma$-overfitting and elaborate further on this phenomenon on ImageNet-100 in Sec. C.

**Data augmentation experiments.** We emphasize that when considering the AugMix method, we only use the data augmentation provided by the authors, and we do not use the regularization term based on the Jensen-Shannon divergence that the authors also propose. We note that this latter regularization could potentially improve all data augmentation methods, and not only the AugMix augmentation. For the experiments that involve training on Stylized ImageNet, we use in each batch 28 stylized images and 100 standard ImageNet images following Rusak et al. (2020). ANT (Rusak et al., 2020) is the only exception where instead of training from a random initialization, we follow the scheme of the authors and fine-tune a standardly pretrained ImageNet-100 model. Additionally, we note that the noise generator of Rusak et al. (2020) uses skip connections with Gaussian noise and experience replay of previous noise generators. This means that there is a certain Gaussian noise component in the final noise which implies that it partially overlaps with the common corruptions from CIFAR-10-C and ImageNet-100-C.

**Runtime of Relaxed LPIPS AT.** We report a full runtime comparison between standard training, $\ell_2 / \ell_\infty$ adversarial training, RLAT, and Fast PAT in Table 8. The main observation is that RLAT is significantly faster than Fast PAT and leads only to a slight overhead compared to $\ell_2/\ell_\infty$ adversarial training.

# B   Ablation study for AdvProp and adversarial training

In this section, we provide experimental details for the AdvProp baseline and compare it with the standard $\ell_\infty$ adversarial training.

AdvProp (Xie et al., 2020) is a method based on adversarial training where the objective consists of a mixture of clean and adversarial examples for which separate BatchNorm layers are used, and only the clean BatchNorm layers are used at test time. This method was shown to improve the accuracy on clean images compared to standard adversarial training and to help to generalize under distribution shifts such as common corruptions, so we consider it here in more detail. As shown in Table 3, AdvProp achieves 94.7% standard accuracy and 82.9% common corruption accuracy. Thus AdvProp performs comparably to 100% $\ell_\infty$ adversarial training (82.9% vs 82.7% accuracy on CIFAR-10-C), however, AdvProp still performs worse than 100% $\ell_2$ adversarial training (83.4%) and 100% RLAT (84.1%).
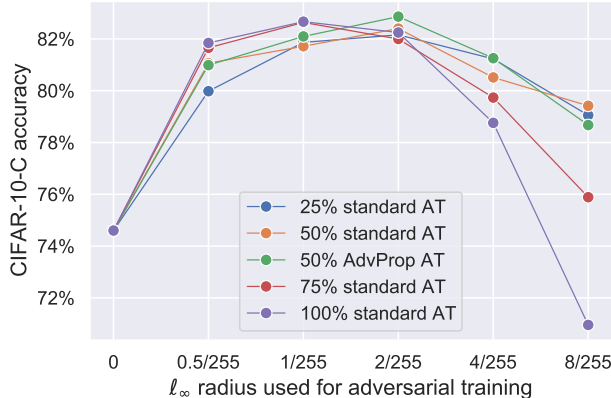
Figure 6: Accuracy on common corruptions from CIFAR-10-C for ResNet-18 models adversarially trained using different $\ell_\infty$ radii and different proportions of adversarial and clean examples together with the AdvProp scheme.

In Fig. 6, we show the results of an ablation study for PreAct ResNet-18 models adversarially trained using different $\ell_\infty$ radii and different proportions of adversarial and clean examples (25%, 50%, 75%, 100%) together with the AdvProp scheme. We can see that AdvProp outperforms 100% standard AT but only by a small margin (+0.2%). Moreover, 100% standard AT performs comparably to 75% standard AT and better than 50% and 25% standard AT. Thus, we observe no benefit in mixing clean and adversarial samples for standard AT unlike for Gaussian data augmentation. We emphasize here that the advantage of the standard $\ell_p$ adversarial training is that it is a conceptually simpler method as it does not require using separate BatchNorms during training, and balancing clean and adversarial samples. Besides, AdvProp requires up to 50% more training time if the same number of adversarial examples is used as for 100% standard AT.

## C Details on $\sigma$-overfitting

In this section, we provide experiments related to the $\sigma$-overfitting phenomenon on ImageNet-100 and provide a further discussion on it.

**$\sigma$-overfitting on ImageNet.** On ImageNet-100-C, the gap between 50% Gaussian augmentation and 100% Gaussian augmentation is even larger than on CIFAR-10-C (see Table. 4). To study the $\sigma$-overfitting phenomenon in more detail, we repeat the experiment behind Fig. 3 on ImageNet-100 and show the results in Fig. 7.

We first focus on large Gaussian perturbations (up to $\sigma = 1$ for image pixels in $[0, 1]$) in Fig. 7 (a). We observe that 100% Gaussian augmentation *severely* overfits to the noise magnitude used for training while the 50% Gaussian augmentation scheme mitigates this problem. However, 50% Gaussian augmentation does not completely solve the $\sigma$-overfitting problem since we observe that the loss still has a local maximum around $\sigma = 0.2$ (with a $\approx 1.6\times$ increase compared to the loss at $\sigma = 0.45$). Therefore, 50% Gaussian augmentation may be a suboptimal method against $\sigma$-overfitting. We believe that future research is needed to better understand improved mitigation strategies.

We additionally plot the performance of standard and $\ell_2$ adversarially trained models for a

(a) A larger range of the standard deviation $\sigma \in [0,1]$      (b) A smaller range of the standard deviation $\sigma \in [0, 0.1]$
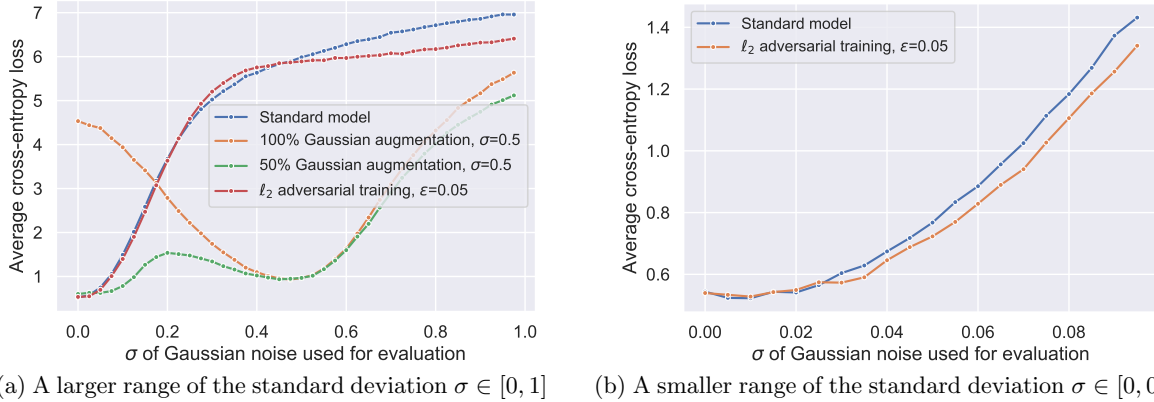
Figure 7: The cross-entropy loss under Gaussian noise of different training methods for ImageNet-100. We see that 100% Gaussian augmentation *severely* overfits to the noise magnitude used for training while the 50% Gaussian augmentation scheme mitigates this problem, but not completely, since it has a noticeable local maximum $\sigma = 0.2$, and $\ell_2$ adversarial training does not suffer from this problem.

smaller range of Gaussian perturbations with $\sigma \in [0, 0.1]$ in Fig. 7 (b). We can observe that there is no $\sigma$-overfitting trend for standard and $\ell_2$ adversarially trained models. Moreover, the latter has a slightly smaller loss for small values of $\sigma$.

**Ford et al. (2019) in the context of $\sigma$-overfitting.** As a Gaussian data augmentation baseline, Ford et al. (2019) use a scheme that is actually different from both 50% and 100% Gaussian augmentation schemes. They perform Gaussian augmentation on *each* sample, however they sample the standard deviation uniformly at random from the range $[0, \sigma]$[5]. This strategy can be seen as an interpolation between the 50% and 100% Gaussian augmentation schemes. Moreover, another difference in the results from Ford et al. (2019) compared to our paper is that they computed corruptions for ImageNet-C in-memory which leads to some discrepancy compared to static images (e.g., see Fig. 5 in Ford et al. (2019) for an illustration).

**$\sigma$-overfitting and adversarial training.** As we can see from Fig. 3 and Fig. 7, adversarial training does not suffer from the $\sigma$-overfitting problem which may explain why applying 50% adversarial training (as in Section B) does not lead to better results compared to 100% adversarial training. We believe that the difference between Gaussian augmentation and adversarial training can occur due to a much larger norm of the perturbation used for data augmentation. On CIFAR-10-C, the optimal $\ell_2$ radius for adversarial training is 0.1 while the norm of Gaussian vectors is approximately $\sigma_{100\%} \cdot \sqrt{d} = 0.05 \cdot \sqrt{32 \cdot 32 \cdot 3} \approx 2.77$ for 100% Gaussian augmentation and $\sigma_{50\%} \cdot \sqrt{d} = 0.1 \cdot \sqrt{32 \cdot 32 \cdot 3} \approx 5.54$ for 50% Gaussian augmentation. It is therefore likely that due to a much larger norm of the perturbation, the model trained with 100% Gaussian noise fails to generalize to perturbations of smaller norms, while this failure can be alleviated to some extent by using the 50% scheme. On a related note, some variations of adversarial training are known to suffer from a phenomenon called *catastrophic overfitting* (Tramèr et al., 2018; Wong et al., 2020). Catastrophic overfitting shares some similarities with $\sigma$-overfitting, in the sense that the model

---

[5]We confirmed this implementation detail via private communication with the authors. Note that this also corresponds to what (Rusak et al., 2020) report in Appendix H.

overfits to a particular perturbation type used during training. Clarifying the relation of catastrophic overfitting and $\sigma$-overfitting is an interesting direction for future work.

# D  Details on the relaxed LPIPS adversarial training

In this section, we first discuss in more detail the approach of Laidlaw et al. (2021), then present complete derivations for RLAT where LPIPS is defined using multiple layers, discuss implementation details of RLAT, and evaluate the $\ell_2$ robustness of RLAT and a few other baselines.

**Details on the perceptual attacks of Laidlaw et al. (2021).**  At each step of the Perceptual Projected Gradient Descent (PPGD) proposed in Laidlaw et al. (2021), both the loss $\ell$ and the neural network $f$ used to define $\mathrm{d_{LPIPS}}$ are linearized, and the constrained problem (4) is approximated with a large linear system which is solved approximately with $K$ iterations of the conjugate gradient method. To satisfy the constraint in (4), the solution $\delta$ is then approximately projected onto the LPIPS-ball, i.e. onto the set $\{\delta : \mathrm{d_{LPIPS}}(x, x + \delta) \leq \varepsilon\}$, for which $n$ iterations of the bisection method are used. For $T$ iterations of PPGD, the algorithm in total requires $T(K + n + 4)$ forward passes and $T(K + n + 3)$ backward passes of the network which makes it significantly more expensive than standard PGD which requires $T$ forward and backward passes.

The Lagrangian Perceptual Attack (LPA) uses the following Lagrangian relaxation of the objective:

$$\max_\delta \ell(x + \delta, y; \theta) - \lambda \max\{\mathrm{d_{LPIPS}}(x, x + \delta) - \varepsilon, 0\},$$

which is solved by gradient descent for several values of the Lagrange multiplier $\lambda$ (usually $S = 5$ in their experiments) and whose solution is then projected back onto the LPIPS-ball. In total, the attack requires $2ST + n + 2$ forward passes and $ST + n + 2$ backward passes of the network which also makes it expensive due to the outer loop over $S$ different values of $\lambda$.

These two attacks are too computationally expensive to be efficiently used during adversarial training. To speed up the method, they additionally propose Fast-LPA where $\lambda$ is not searched over but is instead increased during the training according to a fixed schedule and no projection steps are included. Then Fast-LPA requires $2T + 1$ forward and $T + 1$ backward passes that represent a small overhead compared to PGD but a large one when compared to single-step methods such as FGSM. We note that the possibility of using Fast-LPA with a few iterations is worth investigating in future work, although it appears to be not straightforward because of the Lagrangian formulation and the need to tune the parameter $\lambda$ over iterations of Fast-LPA.

**Relaxation for multi-layer LPIPS.**  We derive here the relaxation of LPIPS adversarial training for a general *multi-layer* version of the LPIPS distance. We recall from Eq. (3) that the LPIPS distance can be written as

$$\mathrm{d_{LPIPS}}(x, x + \delta)^2 = \sum_{l=1}^{L} \alpha_l \|\phi_l(x) - \phi_l(x + \delta)\|_2^2.$$

We use the convention that $\alpha_l = 0$ if a layer $l$ is not in the set of the layers used in the LPIPS distance, i.e. if $l \notin \mathcal{L}_{LPIPS}$. We consider the network $f$ written in its compositional form, i.e.,

$f(x) = g_L \circ \cdots \circ g_1(x)$. The LPIPS adversarial problem defined in Eq. 4 is then equivalent to the problem

$$\max_{\delta} \quad \ell(g_L(\ldots g_1(x + \delta) \ldots))$$

$$\text{s.t.} \quad \sum_{l=1}^{L} \alpha_l \left\| \phi_l(x) - \phi_l(x + \delta) \right\|_2^2 \leq \varepsilon^2 \,.$$

We introduce the slack variables $\tilde{\delta}^{(l)}$ for $l = 1, \ldots, L$, defined as $\tilde{\delta}^{(l)} = g_l(g_{l-1}(\ldots g_1(x + \tilde{\delta}^{(1)}) \ldots) + \tilde{\delta}^{(l-1)})g_l(\ldots g_1(x) \ldots)$ when $l \in \mathcal{L}_{LPIPS}$ and $\tilde{\delta}^{(l)} = 0$ otherwise. The previous problem can be written as:

$$\max_{\tilde{\delta}^{(1)}, \ldots, \tilde{\delta}^{(L)}} \quad \ell(g_L(\ldots g_1(x + \tilde{\delta}^{(1)}) \cdots + \tilde{\delta}^{(L)}))$$

$$\text{s.t.} \quad \sum_{l=1}^{L} \alpha_l \left\| \tilde{\delta}^{(l)} \right\|_2^2 \leq \varepsilon^2,$$

$$\tilde{\delta}^{(l)} = g_l(g_{l-1}(\ldots g_1(x + \tilde{\delta}^{(1)}) \ldots) + \tilde{\delta}^{(l-1)}) - g_l(\ldots g_1(x) \ldots) \quad \forall l \in \mathcal{L}_{LPIPS},$$

$$\tilde{\delta}^{(l)} = 0 \quad \forall l \notin \mathcal{L}_{LPIPS}.$$

When relaxing the equality constraints on the slack variables $\tilde{\delta}^{(l)}$ for $l \in \mathcal{L}_{LPIPS}$ we obtain the following relaxation

$$\max_{\tilde{\delta}^{(1)}, \ldots, \tilde{\delta}^{(L)}} \quad \ell(g_L(\ldots g_1(x + \tilde{\delta}^{(1)}) \cdots + \tilde{\delta}^{(L)}))$$

$$\text{s.t.} \quad \sum_{l=1}^{L} \alpha_l \left\| \tilde{\delta}^{(l)} \right\|_2^2 \leq \varepsilon^2,$$

$$\tilde{\delta}^{(l)} = 0 \quad \forall l \notin \mathcal{L}_{LPIPS}.$$

We further relax the inequality constraint on $\sum_{l=1}^{L} \alpha_l \left\| \tilde{\delta}^{(l)} \right\|_2^2$ as individual constraints on each $\left\| \tilde{\delta}^{(l)} \right\|_2$ in the following way

$$\max_{\tilde{\delta}^{(1)}, \ldots, \tilde{\delta}^{(L)}} \quad \ell(g_L(\ldots g_1(x + \tilde{\delta}^{(1)}) \cdots + \tilde{\delta}^{(L)}))$$

$$\text{s.t.} \quad \left\| \tilde{\delta}^{(l)} \right\|_2 \leq \frac{\varepsilon}{\sqrt{\alpha_l}} \quad \forall l \in \mathcal{L}_{LPIPS},$$

$$\tilde{\delta}^{(l)} = 0 \quad \forall l \notin \mathcal{L}_{LPIPS}.$$

Denoting by $\varepsilon_l = \frac{\varepsilon}{\sqrt{\alpha_l}}$, we finally obtain the RLAT relaxation from Eq. 6

$$\max_{\tilde{\delta}^{(1)}, \ldots, \tilde{\delta}^{(L)}} \quad \ell(g_L(\ldots g_1(x + \tilde{\delta}^{(1)}) \cdots + \tilde{\delta}^{(L)})) \tag{7}$$

$$\text{s.t.} \quad \| \tilde{\delta}^{(l)} \|_2 \leq \varepsilon_l \quad \forall l \in \mathcal{L}_{LPIPS},$$

$$\tilde{\delta}^{(l)} = 0 \quad \forall l \notin \mathcal{L}_{LPIPS}.$$

**Algorithm 1:** Single iteration of relaxed LPIPS adversarial training (RLAT)

**input** : network weights $\theta$, batch of training samples $(x_i, y_i)_{i=1}^b$
**output** : updated network weights $\theta_{new}$

1 **for** $i$ **in** $\{1, \ldots, b\}$ **do**
2 $\quad$ $\forall l \in \{1, \ldots, L\}$: $\tilde{\delta}_i^{(l)} := 0$
3 $\quad$ **for** $l$ **in** $\mathcal{L}_{LPIPS}$ **do**
4 $\quad\quad$ $\nabla_i^{(l)} := \nabla_{\tilde{\delta}_i^{(l)}} \ell(g_L(\ldots g_1(x_i + \tilde{\delta}_i^{(1)}) \cdots + \tilde{\delta}_i^{(L)}), y_i)$
5 $\quad$ **for** $l$ **in** $\mathcal{L}_{LPIPS}$ **do**
6 $\quad\quad$ $\tilde{\delta}_i^{(l)} := \varepsilon_l \nabla_i^{(l)} / \left\| \nabla_i^{(l)} \right\|_2$
7 $\theta_{new} := \theta - \eta \nabla_\theta \frac{1}{b} \sum_{i=1}^b \ell(g_L(\ldots g_1(\Pi_{[0,1]^d}[x_i + \tilde{\delta}_i^{(1)}]) \cdots + \tilde{\delta}_i^{(L)}), y_i)$
8 **return** $\theta_{new}$

We provide the algorithm for a single iteration of weight updates for RLAT in Algorithm 1. We show the weight update for standard SGD but any other optimizer can be used as well. We emphasize that one of the important advantages of RLAT is its computational efficiency since it leads to only $2\times$ overhead since we can successfully use a single-step adversarial training for it (see Fig. 5 for LPIPS robustness evaluation with an iterative attack). We refer to Table 8 for exact timings and comparison to Fast PAT and other methods.

**Layer selection.** We choose to use the following layers for LPIPS used for RLAT: input, conv1, conv2_x, conv3_x, conv4_x, and conv5_x. We tried various combinations of layers including all layers in the network, all BatchNorm layers, and all convolution layers, and the best results were obtained when perturbations are added to the outputs of residual blocks and the first convolution layer.

**Magnitude of layerwise perturbations.** Similarly to $\{\alpha_l\}_{l=1}^L$ in the definition of the LPIPS distance in Eq. (3), the constraints $\{\varepsilon_l\}_{l=1}^L$ for different layers in Eq. (7) also need to be carefully selected so that the perturbation magnitudes on different layers are balanced. Our final approach sets the layerwise bounds $\varepsilon_l$ proportionally to the layer's dimensionality and depth:

$$\varepsilon_l = \frac{1}{l} \frac{d_l}{d_{in}} \varepsilon,$$

where $d_l$ is the dimension of the $l$-th feature maps and $d_{in}$ is the input dimension. We choose this scaling since it is simple enough and empirically more effective than other simple scaling methods that we have tried such as the constant or inverse proportional strategies, or even more involved methods such as dynamic adjusting of the scale to the average of the layer's BatchNorm.

**$\ell_2$ robustness of RLAT.** To complement the LPIPS robustness evaluation in Fig. 5, we also report the $\ell_2$ robustness of the same set of models in Fig. 8: standard, $\ell_2$ AT, Fast perceptual AT, and RLAT models with their main hyperparameters selected to perform best on common corruptions. We evaluate $\ell_2$ robustness using the APGD-CE attack with 100 iterations and 5 random restarts (Croce & Hein, 2020) for different $\ell_2$ radii $\varepsilon \in \{0.05, 0.1, 0.25, 0.5\}$. We observe that *all* three adversarial training methods improve the $\ell_2$ robustness substantially compared to the standard model.
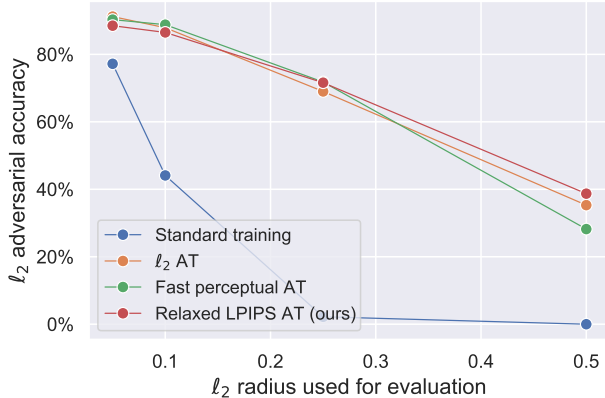
Figure 8: $\ell_2$ adversarial robustness of different training schemes on CIFAR-10. All three adversarial training methods improve the $\ell_2$ robustness substantially compared to the standard model.

# E    Performance under various distribution shifts

In this section, we provide additional experiments on distribution shifts that are different from the common corruptions that we studied throughout this paper.

For this, we use three distribution shifts to evaluate our models: ImageNet-A, ImageNet-R, and Stylized ImageNet (SIN). We report the results in Table 9 where we compute the accuracy on Stylized ImageNet on all 100 classes, and the accuracy on ImageNet-A and ImageNet-R on all classes that overlap with the classes of ImageNet-100. We use the same models for this evaluation as the ones reported in Table 4, i.e. these models have been selected after a grid search to maximize the performance on ImageNet-100-C. We observe that for evaluations on ImageNet-100-A and Stylized ImageNet-100, RLAT moderately improves the accuracy ($+0.4\%$ and $+1.1\%$ respectively) but does not yield improvements on ImageNet-100-R ($-0.1\%$). As expected, training on SIN gives very significant improvements for an evaluation on SIN since the same distribution was used during training and testing. We also note that the performance of all methods could be improved if the model selection was performed on the target datasets, and not on ImageNet-100-C. Finally, we observe that for some data augmentation methods like AugMix and SIN, using RLAT leads to further improvements, e.g. from $35.1\%$ to $37.0\%$ for SIN + RLAT on ImageNet-100-R. Overall, we conclude that there is no method that performs best on all distribution shifts, and the obtained improvements are relatively small unless one uses a target distribution shift for training.

# F    Supplementary figures and tables

In this section, we present additional experimental results related to Sections 4 and 6.

**Performance of different methods across individual corruptions.**  First, we show the performance of the simple baselines considered in Section 4 over each of the 15 corruptions of CIFAR-10-C. We show in Fig. 9 the error rates of the standard and the $\ell_2$ adversarially trained models and in Fig. 10 a breakdown of the accuracy of all simple baselines (i.e., standard and $\ell_2$ adversarially trained models, together with the models trained with gradient regularization and Gaussian data augmentation). We first note that $\ell_2$ adversarial training leads to better average

Table 9: Accuracy of various methods on different distribution shifts: ImageNet-100-A, ImageNet-100-R, and Stylized ImageNet-100. Gray-colored numbers correspond to models trained and evaluated using Stylized ImageNet.

| Method | Standard | IN-100-A | IN-100-R | IN-100-Stylized |
|---|---|---|---|---|
| Standard training | **86.6%** | 5.9% | 33.2% | 16.6% |
| 100% Gaussian augmentation | 86.4% | 5.8% | 31.2% | 17.1% |
| 50% Gaussian augmentation | 83.8% | 5.7% | 32.6% | **18.9%** |
| Fast PAT | 71.5% | 5.4% | **34.6%** | 17.7% |
| $\ell_\infty$ AT | 86.5% | 5.0% | 33.2% | 18.1% |
| $\ell_2$ AT | 86.3% | 5.5% | 33.2% | 17.7% |
| Relaxed LPIPS AT | 86.5% | **6.3%** | 33.1% | 17.7% |
| AugMix (no JSD loss) | 86.7% | **5.5%** | 31.5% | 20.1% |
| AugMix (no JSD loss) + Relaxed LPIPS AT | **86.8%** | 5.1% | **33.2%** | **20.6%** |
| Stylized ImageNet | **86.6%** | **6.5%** | 35.1% | 62.5% |
| Stylized ImageNet + Relaxed LPIPS AT | 86.5% | **6.5%** | **37.0%** | **63.4%** |
| ANT$^{3x3}$ | **85.9%** | **5.6%** | **33.3%** | **20.8%** |
| ANT$^{3x3}$ + Relaxed LPIPS AT | 85.3% | 5.3% | 32.8% | 20.7% |

performance compared to other baselines, and improves on each corruption type (blurs, digital, noises, weather) and particularly on JPEG compression, elastic transform, pixelate, and zoom blur. However, compared to the standard model, adversarial training worsens the performance on contrast and fog, and slightly on brightness as has been observed in previous work for $\ell_\infty$ adversarial training with a large $\varepsilon = 8/255$ (Ford et al., 2019). Moreover, Fig. 9 complements Fig. 4 and helps to motivate why the LPIPS distance can be more suitable than the $\ell_2$ distance for the problem of being robust to common corruptions (see the discussion in Sec. 5.1).

We additionally compare these baselines together with 50% Gaussian augmentation, AdvProp and RLAT in Table 10. We observe that RLAT leads to better average performance than other baselines (not taking into account 50% Gaussian augmentation since it is partially trained with a corruption from CIFAR-10-C) and consistently improves upon $\ell_2$ adversarial training. AdvProp helps for the snow and elastic transform corruptions, has a better behavior on corruptions on which $\ell_2$/RLAT adversarial training and Gaussian augmentation perform poorly (such as brightness, fog, or contrast) but performs suboptimally on noise. Finally, 50% Gaussian augmentation obtains high accuracy, consistently improving upon 100% Gaussian augmentation (in particular on blur corruptions) due to its usage of clean samples which mitigates $\sigma$-overfitting.

**Detailed performance of $\ell_2$ adversarial training trained with different $\varepsilon$.** We study further the influence of the radius $\varepsilon$ on the performance of $\ell_2$ adversarial training on CIFAR-10-C. We present in Table 11 the accuracy of $\ell_2$ adversarially trained model, trained with different values of $\varepsilon$. Interestingly, Table 11 suggests that the same degradation for fog and contrast occurs even for the *smallest* $\varepsilon$ used for training. We also observe that different corruptions require different $\varepsilon$ for optimal performance. In particular, the optimal $\varepsilon$ for the frost corruptions is 0.05 while for impulse noise the optimal $\varepsilon$ is an order of magnitude larger, i.e. 0.5. Despite being widely used in the literature on $\ell_2$ robustness, $\varepsilon = 0.5$ is suboptimal for many other corruptions, and the optimal average performance over *all* corruptions for a single model is obtained at $\varepsilon = 0.1$.

Figure 9: Error rates of a standard and $\ell_2$ adversarially trained models on different common corruptions from CIFAR-10-C.



Figure 10: Accuracy for different individual corruptions on CIFAR-10-C. $\ell_2$ adversarial training leads to better average performance compared to other baselines.

**Average perturbation distance for different corruptions.** In Table 12 we report the average distances between clean and corrupted images for the LPIPS and $l_2$ norms which is the same data as in Fig. 4. We report exact numbers to further illustrate the point that adversarial training with worst-case perturbations in a *small $\ell_2$ ball* (such as $\varepsilon = 0.1$) leads to robustness against corruptions of a much larger magnitude. We can observe from Table 12 that for some corruptions, the perturbation norm does not grow monotonically (particularly, glass blur and elastic transform) which we highlight in **red**. We observe that for the LPIPS distance such behavior occurs less often. Another observation is that the $l_2$ distance itself does not always accurately reflects the strength of the performance degradation. For example, fog and brightness have similar magnitude (and the largest among the other corruptions), but very different behavior in terms of accuracy: degradation under fog is much higher than under brightness.

Table 10: Accuracy of clean training, gradient regularization, 100% and 50% Gaussian data augmentation, AdvProp, $\ell_2$ adversarial training, and RLAT on CIFAR-10-C using ResNet-18. Gray-colored numbers correspond to methods that were at least partially trained with the corruptions from CIFAR-10-C.

| Corruption | Clean | GradReg | 100% Gauss | 50% Gauss | AdvProp | $\ell_2$ AT | RLAT |
|---|---|---|---|---|---|---|---|
| Shot noise | 60.1% | 75.1% | 89.2% | **91.2%** | 82.0% | 86.4% | 88.8% |
| Motion blur | 79.1% | 78.9% | 72.0% | 82.2% | 82.2% | **82.3%** | **82.3%** |
| Snow | 82.8% | 82.8% | 86.0% | 85.9% | **86.9%** | 86.6% | 86.2% |
| Pixelate | 76.7% | 79.8% | 87.4% | 87.7% | 87.7% | 89.9% | **90.2%** |
| Gaussian noise | 47.1% | 67.6% | 87.8% | 90.8% | 77.0% | 83.4% | **86.0%** |
| Defocus blur | 83.8% | 83.9% | 78.8% | 86.5% | 87.1% | 87.1% | **87.2%** |
| Brightness | **93.3%** | 91.9% | 91.0% | 91.2% | 92.8% | 92.0% | 91.5% |
| Fog | **88.5%** | 83.1% | 71.5% | 78.7% | 88.2% | 77.5% | 76.7% |
| Zoom blur | 79.7% | 81.4% | 76.0% | 85.2% | 85.8% | 86.0% | **86.1%** |
| Frost | 80.6% | 83.0% | **87.2%** | **87.2%** | 86.4% | 86.9% | 87.0% |
| Glass blur | 56.6% | 63.5% | 76.0% | 79.3% | 74.4% | 77.2% | **80.4%** |
| Impulse noise | 51.4% | 66.1% | 76.8% | **87.3%** | 71.8% | 75.1% | 79.6% |
| Contrast | **76.4%** | 68.1% | 58.4% | 66.3% | 68.6% | 63.5% | 62.6% |
| JPEG compression | 79.3% | 85.3% | 88.6% | 89.8% | 89.8% | 90.2% | **90.5%** |
| Elastic transform | 84.4% | 84.4% | 80.2% | 86.3% | **87.9%** | 86.9% | 87.2% |
| Average | 74.6% | 78.3% | 80.5% | 85.0% | 82.9% | 83.4% | **84.1%** |

**Detailed model comparison for different corruption severity.** In Tables 13 and 14 we report the accuracy of selected models for each corruption level separately. We first note that for all models, as one could expect, the accuracy is gradually decreasing with the corruption severity. When comparing all the baselines, RLAT shows the best accuracy on the majority of corruption levels (three on Imagenet-100 and four on CIFAR-10). It is also worth mentioning that AdvProp on CIFAR-10 works better for smaller corruption levels which can be explained by its higher standard accuracy. On ImageNet-100-C, we can observe that the Fast PAT model has the best accuracy at the highest severity level despite having clearly suboptimal standard accuracy (71.5% compared to 86.6% of the standard model) and average corruption accuracy (45.2% compared to 47.5% of the standard model). We also observe that for the severity level 4, $\ell_2$ adversarial training is slightly better than RLAT (37.0% vs 36.8%). Moreover, we notice that when RLAT is combined with different data augmentation schemes, the improvement is often achieved at multiple severity levels simultaneously. For example, when RLAT is combined with AugMix, the accuracy is improved on all severity levels.

Table 11: Accuracy of $\ell_2$ adversarial training for different $\varepsilon$ on CIFAR-10-C. Similarly to Fig. 1 which was done for $\ell_\infty$ norm, we observe here that the widely used $\ell_2$ radius $\varepsilon = 0.5$ leads to suboptimal corruption accuracy.

| | | | | Radius $\varepsilon$ used for $\ell_2$ adversarial training | | | | | |
|---|---|---|---|---|---|---|---|---|---|
| Corruption | $\varepsilon = 0$ | $\varepsilon = 0.01$ | $\varepsilon = 0.05$ | $\varepsilon = 0.08$ | $\varepsilon = 0.1$ | $\varepsilon = 0.15$ | $\varepsilon = 0.2$ | $\varepsilon = 0.5$ | $\varepsilon = 1$ |
| Shot noise | 60.1% | 70.6% | 81.6% | 84.9% | 86.4% | **87.0%** | 86.9% | 85.1% | 79.6% |
| Motion blur | 79.1% | 79.4% | 81.4% | 81.8% | **82.3%** | 82.1% | 82.0% | 80.0% | 75.3% |
| Snow | 84.7% | 82.8% | 86.6% | **86.9%** | 86.6% | 86.0% | 85.5% | 81.3% | 75.0% |
| Pixelate | 76.7% | 82.0% | 88.8% | 89.7% | 89.9% | **90.2%** | 89.7% | 86.5% | 81.2% |
| Gaussian noise | 47.1% | 59.6% | 76.0% | 81.3% | 83.4% | 84.6% | **85.1%** | 83.8% | 78.4% |
| Defocus blur | 83.8% | 84.5% | 86.2% | 86.7% | **87.1%** | 86.8% | 86.5% | 83.7% | 78.6% |
| Brightness | **93.3%** | 93.2% | 93.0% | 92.5% | 92.0% | 91.3% | 90.2% | 85.4% | 79.0% |
| Fog | **88.5%** | 86.7% | 80.8% | 78.5% | 77.5% | 74.4% | 71.5% | 61.5% | 54.1% |
| Zoom blur | 79.7% | 81.9% | 84.7% | 85.6% | **86.0%** | 85.7% | 85.4% | 82.7% | 77.8% |
| Frost | 80.6% | 84.4% | **87.5%** | **87.5%** | 86.9% | 86.4% | 85.7% | 79.7% | 71.5% |
| Glass blur | 56.6% | 62.7% | 72.9% | 76.1% | 77.2% | 80.7% | **81.6%** | 81.5% | 76.7% |
| Impulse noise | 51.5% | 58.7% | 66.4% | 73.2% | 75.1% | 76.5% | 78.1% | **79.7%** | 75.0% |
| Contrast | **76.4%** | 72.3% | 65.9% | 63.7% | 63.5% | 61.1% | 59.3% | 50.5% | 44.0% |
| JPEG compression | 79.3% | 86.0% | 89.9% | **90.4%** | 90.2% | 90.3% | 89.9% | 86.7% | 81.5% |
| Elastic transform | 84.4% | 85.7% | **87.2%** | **87.2%** | 86.9% | 86.6% | 85.9% | 82.4% | 77.1% |
| Average | 74.6% | 78.2% | 81.9% | 83.1% | **83.4%** | 83.3% | 82.9% | 79.4% | 73.7% |

Table 12: Average $\ell_2$ and LPIPS distance for different corruptions and severity levels from CIFAR-10-C. Note that the distances do not always monotonically increase with the corruption level. We mark such cases in **red** and observe that they occur less often for LPIPS than for the $\ell_2$ distance.

| | $\ell_2$ distance at different severity levels | | | | | LPIPS distance at different severity levels | | | | |
|---|---|---|---|---|---|---|---|---|---|---|
| Corruption | 1 | 2 | 3 | 4 | 5 | 1 | 2 | 3 | 4 | 5 |
| Shot noise | 1.67 | 2.35 | 3.68 | 4.22 | 5.13 | 0.089 | 0.143 | 0.245 | 0.284 | 0.341 |
| Motion blur | 2.40 | 3.51 | 4.33 | 4.32 | 4.97 | 0.059 | 0.114 | 0.166 | 0.166 | 0.211 |
| Snow | 2.92 | 5.83 | 6.60 | 9.10 | 12.17 | 0.068 | 0.155 | 0.160 | 0.188 | 0.227 |
| Pixelate | 1.25 | 1.77 | 1.97 | 2.48 | 3.04 | 0.130 | 0.060 | 0.074 | 0.138 | 0.202 |
| Gaussian noise | 2.19 | 3.26 | 4.31 | 4.83 | 5.34 | 0.027 | 0.217 | 0.294 | 0.328 | 0.359 |
| Defocus blur | 0.43 | 1.06 | 1.61 | 2.09 | 2.98 | 0.003 | 0.019 | 0.048 | 0.085 | 0.153 |
| Brightness | 2.26 | 4.59 | 6.85 | 9.01 | 12.95 | 0.006 | 0.022 | 0.045 | 0.071 | 0.132 |
| Fog | 2.81 | 5.54 | 7.18 | 8.45 | 10.20 | 0.022 | 0.086 | 0.147 | 0.215 | 0.332 |
| Zoom blur | 3.04 | 3.56 | 4.20 | 4.83 | 5.40 | 0.079 | 0.094 | 0.124 | 0.153 | 0.189 |
| Frost | 6.86 | 10.14 | 11.39 | 10.45 | 10.26 | 0.077 | 0.141 | 0.208 | 0.214 | 0.266 |
| Glass blur | 4.70 | 4.64 | 4.27 | 6.73 | 6.28 | 0.253 | 0.248 | 0.235 | 0.333 | 0.321 |
| Impulse noise | 3.08 | 4.37 | 5.35 | 6.92 | 8.20 | 0.136 | 0.223 | 0.289 | 0.387 | 0.452 |
| Contrast | 2.80 | 5.60 | 6.71 | 7.83 | 9.51 | 0.020 | 0.092 | 0.143 | 0.216 | 0.386 |
| JPEG compression | 1.59 | 1.95 | 2.07 | 2.20 | 2.38 | 0.073 | 0.108 | 0.121 | 0.134 | 0.153 |
| Elastic transform | 7.37 | 6.79 | 6.11 | 5.67 | 4.76 | 0.168 | 0.152 | 0.151 | 0.175 | 0.198 |

Table 13: Accuracy of different methods on CIFAR-10-C. Gray-colored numbers correspond to methods that were at least partially trained with the corruptions from CIFAR-10-C.

| Method | Standard | Accuracy at different severity levels | | | | | |
| --- | --- | --- | --- | --- | --- | --- | --- |
| | | 1 | 2 | 3 | 4 | 5 | Average |
| Standard training | 95.1% | 87.6% | 82.3% | 76.2% | 69.2% | 57.9% | 74.6% |
| Gradient regularization | 93.4% | 87.9% | 84.9% | 81.0% | 74.8% | 65.5% | 78.8% |
| 100% Gaussian augmentation | 92.5% | 89.2% | 86.3% | 82.3% | 76.4% | 68.1% | 80.5% |
| 50% Gaussian augmentation | 93.2% | 91.0% | 89.1% | 86.8% | 82.6% | 75.8% | 85.0% |
| Fast PAT | 93.4% | 89.5% | 87.2% | 83.7% | 79.0% | 72.6% | 82.4% |
| $\ell_\infty$ AT | 93.3% | 90.8% | 88.3% | 84.5% | 78.5% | 71.2% | 82.7% |
| AdvProp | 94.7% | **91.5%** | 88.9% | 85.2% | 79.2% | 69.5% | 82.9% |
| $\ell_2$ AT | 93.6% | 91.1% | 88.8% | 85.5% | 79.8% | 71.8% | 83.4% |
| Relaxed LPIPS AT | 93.1% | 91.1% | **89.0%** | **85.9%** | **80.9%** | **73.5%** | **84.1%** |
| AugMix (no JSD loss) | 95.0% | 92.2% | 90.5% | 88.5% | 84.7% | 78.8% | 86.9% |
| AugMix (no JSD loss) + Relaxed LPIPS AT | 94.8% | **93.1%** | **91.8%** | **90.3%** | **87.0%** | **80.6%** | **88.5%** |

Table 14: Accuracy of different methods on ImageNet-100-C. Gray-colored numbers correspond to methods that were at least partially trained with the corruptions from ImageNet-100-C.

| Method | Standard | Accuracy at different severity levels | | | | | |
| --- | --- | --- | --- | --- | --- | --- | --- |
| | | 1 | 2 | 3 | 4 | 5 | Average |
| Standard training | 86.6% | 70.9% | 58.7% | 47.3% | 35.2% | 25.4% | 47.5% |
| 100% Gaussian augmentation | 86.4% | 70.1% | 57.2% | 46.2% | 34.9% | 25.3% | 46.7% |
| 50% Gaussian augmentation | 83.8% | 73.8% | 65.0% | 56.9% | 45.7% | 34.8% | 55.2% |
| Fast PAT | 71.5% | 61.7% | 52.7% | 45.7% | 36.6% | **29.1%** | 45.2% |
| $\ell_\infty$ AT | 86.5% | 70.6% | 57.9% | 46.5% | 36.2% | 27.4% | 47.7% |
| $\ell_2$ AT | 86.3% | 70.1% | 58.3% | 47.8% | **37.0%** | 27.9% | 48.4% |
| Relaxed LPIPS AT | 86.5% | **71.6%** | **59.6%** | **48.8%** | 36.8% | 27.1% | **48.8%** |
| AugMix (no JSD loss) | 86.7% | 73.9% | 63.3% | 53.9% | 41.1% | 29.5% | 52.3% |
| AugMix (no JSD loss) + Relaxed LPIPS AT | 86.8% | **75.4%** | **65.1%** | **56.2%** | **44.7%** | **32.8%** | **54.8%** |
| Stylized ImageNet | 86.6% | 73.0% | 63.5% | 55.1% | 43.5% | **33.2%** | 53.7% |
| Stylized ImageNet + Relaxed LPIPS AT | 86.5% | **74.1%** | **64.4%** | **56.0%** | **44.1%** | 33.0% | **54.3%** |
| ANT$^{3\text{x}3}$ | 85.9% | 74.2% | **66.5%** | **58.9%** | 49.8% | 39.3% | 57.7% |
| ANT$^{3\text{x}3}$ + Relaxed LPIPS AT | 85.3% | **74.5%** | 66.4% | 58.8% | **50.5%** | **41.2%** | **58.3%** |